

Surveys in Geophysics manuscript No.
(will be inserted by the editor)

The 3D attenuation structure of Deception Island (Antarctica)

J. Prudencio · L. De Siena · J.
M. Ibáñez · E. Del Pezzo · A.
García-Yeguas · A. Díaz-Moreno

Received: date / Accepted: date

J. Prudencio

Instituto Andaluz de Geofísica, University of Granada, Profesor Clavera 12, 18071 Granada,
Spain
Dept. Física Teórica y del Cosmos, University of Granada, Fuentenueva S/N, 18001 Granada,
Spain
INVOLCAN, Antiguo Hotel Taoro, Parque Taoro 22, 38400 Puerto de la Cruz, Tenerife,
Spain
E-mail: janire@ugr.es

L. De Siena

University of Münster, Institut für Geophysik, Correnstrasse 24, Münster, 48149, Germany.
University of Aberdeen, School of Geosciences, Geology and Petroleum Geology, Meston
Building, King's College, Aberdeen AB24 3UE Scotland
Tel. +492518334725
Fax +492518336100
E-mail: lucadesiena@uni-muenster.de

J. M. Ibáñez

Instituto Andaluz de Geofísica, University of Granada, Profesor Clavera 12, 18071 Granada,
Spain
Dept. Física Teórica y del Cosmos, University of Granada, Fuentenueva S/N, 18001 Granada,
Spain
Istituto Nazionale di Geofisica e Vulcanologia, Sezione di Catania -Osservatorio Etneo, 95125
Catania, Italy

E. Del Pezzo

Istituto Nazionale di Geofisica e Vulcanologia, Sezione di Napoli -Osservatorio Vesuviano,
Via Diocleziano 328, 80124 Naples, Italy
Instituto Andaluz de Geofísica, University of Granada, Profesor Clavera 12, 18071 Granada,
Spain

A. García-Yeguas

Dept. Física Aplicada, University of Cádiz, Av. Duque de Nájera 18, 11002, Cádiz, Spain
Instituto Andaluz de Geofísica, University of Granada, Profesor Clavera 12, 18071 Granada,
Spain
INVOLCAN, Antiguo Hotel Taoro, Parque Taoro 22, 38400 Puerto de la Cruz, Tenerife,
Spain

Abstract The seismic and volcanological structure of Deception Island (Antarctica) is an intense focus topic in Volcano Geophysics. The interpretations given by scientists on the origin, nature, and location of the structures buried under the island strongly diverge. We present a high-resolution 3D *P*-wave attenuation tomography model obtained by using the coda normalization method on 20.293 high-quality waveforms produced by active sources. The checkerboard and synthetic anomaly tests guarantee the reproduction of the input anomalies under the island down to a depth of 4 km. The results, once compared with our current knowledge on the geological, geochemical, and geophysical structure of the region, depict Deception as apiecemeal caldera structure leant out of the Bransfield Trough. High attenuation anomalies contouring the north-eastern emerged caldera rim correlate with the locations of sediments. In our interpretation, the main attenuation contrast, which appears under the collapsed southeastern caldera rim, is related to the deeper feeding systems. A unique *P*-wave high attenuation spherical-like anomaly in the inner bay extends between depths of 1 and 3 km. The northern contour of the anomaly coincides with the calderic rim both at 1 and 2 km, while smaller anomalies connect it with deeper structures below 3 km, dipping towards the Bransfield Trough. In our interpretation, the large upper anomaly is caused by a high-temperature shallow (1 to 3 km deep) geothermal system, located beneath the sediment-filled bay in the collapsed blocks and heated by smaller, deeper contributions of molten materials (magma) rising from southeast.

Keywords Attenuation · Scattering · Tomography · Antarctica

1 Introduction

Deception Island (Fig. 1) is considered as a laboratory for Volcano Geophysics due to the large number of multidisciplinary studies focused both on imaging its surface and deep structures and on monitoring its volcanic activity. Scientists have widely studied the origin and morphology of Deception Island, bringing formed general and local models (e.g. Martí et al 1996, 2013; Smellie et al 2002; Fernández-Ibáñez et al 2005; Maestro et al 2007; Barclay et al 2009; Melo et al 2012; Torrecillas et al 2012, 2013). The study of the seismic activity of the volcano is probably the most active and productive research line, as reported by Tejedo et al (2014). There are many results that help to better understand the dynamic and volcanological framework of the area as Vila et al (1992), Almendros et al (1997), Ibáñez et al (1997), Ibáñez et al (2000), Ibáñez et al (2003), Saccorotti et al (2001), Martinez-Arevalo et al

A. Díaz-Moreno

Instituto Andaluz de Geofísica, University of Granada, Profesor Clavera 12, 18071 Granada, Spain

Dept. Física Teórica y del Cosmos, University of Granada, Fuentenueva S/N, 18001 Granada, Spain

INVOLCAN, Antiguo Hotel Taoro, Parque Taoro 22, 38400 Puerto de la Cruz, Tenerife, Spain

(2003), Benitez et al (2007), Carmona et al (2010), Carmona et al (2012), Carmona et al (2014) and García-Yeguas et al (2010). One of the objectives of these seismic studies is to provide 2- or 3-D structure of the area, by using active or passive data as has been done by (Ben-Zvi et al 2009; Zandomeneghi et al 2009; Prudencio et al 2013). These seismic models have been used to confirm or help to built other geophysical or geodynamic models of the island, as magnetotelluric (Pedrera et al 2012), geomagnetic (Muñoz Martín et al 2005), gravimetric (Catalan et al 2006) or geodetic (Berrocoso et al 2012; Prates et al 2013). Additionally, geochemical analysis as the composition and ratio of stable isotopes and gasses produced by fumaroles (Caselli et al 2004, 2007; Kusakabe et al 2009) are also very well know, and provide important information on the presence and origin of magma and fluids. Nowadays with these observables the research community is working to provide a geodynamic and volcanological model that could unify all of them in a single interpretation as those done by (Smellie 2001; Martí et al 2013; Berrocoso et al 2012; Pedrera et al 2012).

The imaging of region-specific velocity and attenuation through direct-wave tomography provides striking results at local, regional, and global scales (e.g. Schurr et al 2003 and Eberhart-Phillips et al 2008). Attenuation tomography is today a standard technique and several codes include this important measurement in their tomographic algorithms (Lees and Lindley 1994; Schurr et al 2003; Hansen et al 2004; Eberhart-Phillips et al 2008; Koulakov et al 2010). Due to the higher sensitivity of the attenuation parameters to the presence of fluids and melt with respect to velocity, attenuation tomography may provide decisive data to discriminate the location and nature of the volcanic and seismic structures under Deception Island.

The modeling of energy (amplitude) propagation in highly-heterogeneous local-scale volcanic media is especially complicated by frequency-dependent source and site effects. In these media, scattering phenomena produce high-frequency long wave-trains of incoherent radiation (coda waves, e.g., Sato et al 2012), affected by dispersion as well as by interference, diffraction, and resonant effects. The coherency in the corresponding direct signals is also quickly lost (La Rocca et al 2001; Chouet 2003; De Siena et al 2013). In these media, we may retrieve P - and S -wave attenuation parameters independently of the site and instrumental transfer functions by using the coda-normalization method (Aki and Richards 1980; Yoshimoto et al 1993; Sato et al 2012). In recent years, this method has been applied to S -wave attenuation tomography at local scale, exploiting the strong scattering effects produced by strong heterogeneity in volcanic regions (Del Pezzo et al 2006; Matsumoto et al 2009; Sato et al 2012; De Siena et al 2010).

The coda-normalization method is based on the equation that correlates the ratio between the S -wave direct energy and the coda-wave energy to the spatial distribution of the inverse total quality factors calculated along the source-station ray-path (Del Pezzo et al 2006; De Siena et al 2009, 2014). If active sources are available, the spatial distribution of P -wave attenuation becomes the only unknown if the final coda-normalization inverse problem, that is, the method may be exploited at best.

In this study, we obtain the P -wave total quality factor (Q_p), which measures the anelastic and scattering losses suffered by P -waves while propagating into the medium. This quantity provides information on the physical, chemical, and geological state of the Earth, and becomes especially useful if compared with seismic velocities. A wide range of physical properties must be considered before discussing the joint results of velocity and attenuation tomography. Their combined interpretation is a decisive tool in discriminating volumes either permeated by fluids or characterized by structural discontinuities (Schurr et al 2003; Eberhart-Phillips et al 2008; De Siena et al 2010).

The relation between velocity and attenuation is often ambiguous. High attenuation and low velocity do not always mean the presence of melt in volcanoes, as fluids, gasses, faults, and, more generally, unconsolidated materials (like sediments) all produce high attenuation in the presence of different velocity signatures (Haberland and Rietbrock 2001; Schurr et al 2003; Hansen et al 2004; De Siena et al 2010; Muksin et al 2013). Several authors (e.g., Priyono et al 2011) suggest that high ΔQ_p^{-1} and low ΔV_p^{-1} in volcanic regions are related to a magmatic system, while others (e.g., Takanami et al 2000) relate these correlation to high-temperature zones without partial melting.

The P -to- S velocity ratio (V_p/V_s) is a decisive parameter to discriminate magma from either fluids or gasses if spatially correlated with high attenuation (Hansen et al 2004; Vanorio et al 2005; De Siena et al 2010; Kuznetsov and Koulakov 2014). Low V_p/V_s anomalies and high attenuation may in fact be associated with the presence of gas filling faults and fractures, hydrothermal basins, and CO_2 emission beneath volcanoes, mountain ranges, and geothermal reservoirs (Julian et al 1996, 1998; Hunsen et al 2004; Hansen et al 2004). The correlation of high V_p/V_s with high attenuation is critical to discriminate fluids from melt. As no V_p/V_s ratio information is available at Deception Island other geophysical, geological, and geochemical information must be considered with care in the final interpretation.

The aim of this study is to obtain reliable 3D frequency-dependent P -wave attenuation images of the upper 4 km beneath Deception Island (South Shetland archipelago, Antarctica) by using a subset of the waveforms employed by Ben-Zvi et al (2009) and Zandomenighi et al (2009) to obtain velocity tomography results. We will provide new evidences that can be used in the future in a new geophysical interpretation by the comparison of the velocity and attenuation results with the current and new scientific results focused on the formation and structure of the Island.

2 Deception Island: volcanological and geophysical models

Deception Island is an active volcanic island composed by rocks that date to less than 0.75 Ma and which suffered several historical eruptions in the last two centuries (Smellie 2001) (Fig. 1). Nowadays its volcanic activity mainly consists of hot hydrothermal waters, fumarolic fields and intense seismic activity composed by volcanic tremor, persistent long-period and volcano-tectonic

103 seismicity (Vila et al 1992; Ortiz et al 1997; Ibáñez et al 2000; Carmona et al
104 2012).

105 As indicated above, many of the present efforts of several researchers are
106 focused in the interpretation of the geophysical, geodetic and geochemical
107 observations in terms of structural and volcanological framework of the vol-
108 cano to understand its past and to infer a possible evolution and volcanic
109 dynamic. These researchers integrated seismic observations, mainly low and
110 high seismic velocities and contrast in attenuation, conductivity, gases and
111 geodetical information. On the base of these observations there are mainly at
112 the present two possible models that are coincident in the interpretation of
113 the shallower structure (0-2 km) and they are in disagree in the interpreta-
114 tion of the deeper structure. In one of them the effects of fractured rocks and
115 the existence of a geothermal system that hydrothermally altered the medium
116 is detected up to 6 km depth (Martí et al 2013). In the other, the observed
117 anomalies are interpreted as the effects of the presence of certain amount of
118 melted rock/material with variable volume (e.g. Ben-Zvi et al 2009; Pedrera
119 et al 2012; Muñoz Martín et al 2005).

120 2.1 Deep Geothermal effect

121 Recently, Martí et al (2013) on the base of new stratigraphy and petrological
122 studies, with the revision of previous results proposed a model of the forma-
123 tion and internal structure of the Island. In reference to the present internal
124 structure, the authors show that a polygonal structural network consisting of
125 several pre-existing major normal faults controlled pre- and post- caldera vol-
126 canism on the island. They defend that the formation of the caldera caused
127 the destruction of the associated magma chamber and hence, recent eruptions
128 have been fed by small batches of deeper-source magma. In their interpreta-
129 tion, a large hydrothermal system developed in the interior of the depression
130 using highly fractured pre-caldera basement and syn-caldera rocks. The au-
131 thors suggested that the current hydrothermal system inside its depression,
132 which may be responsible for most of the present-day observations up to 6 km
133 depth.

134 2.2 Existence of melted material

135 Mostly of the geophysical and geodetic studies performed in the area observed
136 the existence of high contrast of the physical properties studied and these
137 anomalies have an evident presence in the central part of the island (bellow
138 Port Foster). These anomalies extend up to 6-10 km depth and their interpre-
139 tations include the existence of partial melted rocks at depths 2-10 km.

140 **Seismic velocity observations:** Ben-Zvi et al (2009) and Zandomeneghi
141 et al (2009) used the data-set provided by the TOMODEC active seismic
142 experiment to obtain 2D and 3D images of P-wave velocity structure in the

143 entire area of Deception Island between depth of 0 to 10 km. Their results show
144 strong deep (down to 8 km) lateral velocity variations, which are attributed
145 to the presence of crustal magmatic systems with either partial melt regions
146 and frozen intrusive bodies or sediment thickness variations and geothermal
147 systems. The authors indentified a large high-velocity anomaly intersects the
148 northwestern part of Deception Island (Telefon Bay, Fig. 1) taht was associated
149 with the crystalline basement of the South Shetland Island platform. However,
150 the main feature of the velocity models is an extended low P-wave velocity
151 anomaly, which intersects both Port Foster bay and eastern part of the island
152 (Fig. 1). The same authors interpret the shallow how velocity anomalies (0-2
153 km) as the effect of sediment-filled basin, hydrothermal activities, fractured
154 materials from the caldera collapse and others. Ben-Zvi et al (2009) (pp.78) on
155 the base of numerical simulations observed that the velocity anomalies bellow
156 2 km depths are compatible with the presence of partial melted materials (up
157 to 15% melted) and with a maximum volume of up $20km^3$. Zandomeneghi
158 et al (2009) agree this interpretation.

159 **Seismic attenuation observations:** Regarding seismic attenuation, Vila
160 et al (1995) obtained local attenuation parameters from both coda analysis and
161 source parameters information. The authors show abnormally low coda-Q val-
162 ues characterized by high frequency dependence in the inner bay of the island.
163 They do interpret it as due to a hot magmatic intrusion produced during the
164 most recent eruption, but the width of this intrusion is estimated to be only
165 about 0.2 km³. More recently Martinez-Arevalo et al (2003) estimated the
166 seismic attenuation of both P- and S-waves at Deception Island, observing
167 a predominance of scattering- over intrinsic- attenuation. They do interpret
168 these results as produced by a zone of strong heterogeneity, as done in most
169 volcanic areas (Del Pezzo 2008), where the presence of magma patches cannot
170 be excluded. Recently, Prudencio et al (2013) obtained the regional 2D distri-
171 bution of intrinsic and scattering attenuation of the Island by using the same
172 waveform dataset employed to image its velocity structure and the diffusion
173 model. The authors confirm the presence of a high scattering attenuation body
174 below the inner bay of Deception Island, strongly interacting with the coda
175 wave-field, and which may be compatible with the existance of magma.

176 **Gravimetric and magnetotelluric observations:** Muñoz Martín et al
177 (2005) show a very low density anomaly in both magnetic and gravity anomaly
178 maps of Deception Island. The authors interpreted this anomaly as a partially
179 melted intrusive body and they estimated the top of this body at 1.7 km depth
180 using Euler deconvolution techniques. The 3D resistivity models of Pedrera
181 et al (2012) reveal an elongate conductor between 2 and 10 km east of Whalers
182 Bay (Fig. 1), which they interpret as induced by a combination of partial melt
183 and hot fluids. The inferred deep magma sill is connected to the surface by
184 a large resistive path ending Port Foster, interpreted as a shallow magma
185 chamber.

3 Data, method, and inversion setting

3.1 Data and ray tracing.

The waveforms used in this study are a subset of the ones used by Zandomeneghi et al (2009) to obtain 3D velocity images by using a shortest-time ray tracing and a LSQR algorithm inversion. The authors choose two different model parametrizations. The first grid has coarser parametrization (250 m), it is centered on Deception Island and extends 53 km from West to East (WE), 52 km from South to North (SN), and down to 12 km depth. A smaller grid of 100 m step includes Port Foster and the nearest surroundings, and extends 12 km WE, 14 km SN, and down to 7 km depth. In order to compare the velocity and attenuation models we use a grid having the same lateral extension of the first grid in Zandomeneghi et al (2009).

Amplitude data are strongly frequency dependent. We show four recordings produced by a shot in the center of the bay (blue star) and registered at stations M, F, J, and H (Fig. 2). The stations record waveforms with excellent signal-to-noise ratios (larger than 10) for the entire signal above 8 Hz only. However, both Vila et al (1995) and Prudencio et al (2013) show abnormally-low attenuation values at high frequencies in the Port Foster bay, where we focus our attention. Due to this strong attenuation we cannot provide reliable attenuation models of structures as deep as 4 km at frequencies larger than 10 Hz.

We obtain the attenuation model after filtering data in the 4-8 frequency band (6 Hz, central frequency). Considering the lowest measured velocities in the inner bay, the signal wavelength associated with this frequency band safely allows to depict structures of the order of 1 km dimension at 4 km depth. As shown by Prudencio et al (2013) this frequency band also provides stable results for the separate measurements of both intrinsic and scattering attenuation from coda wave data.

We use the same Thurber-modified ray-bending approach described, e.g., by De Siena et al (2010) in the 3D sparse velocity model of Zandomeneghi et al (2009) (Fig. 3). The space density of the rays at depth of 5 km is still sufficient for correctly performing the tomography inversion (Figure 3). On the other hand, observational data associated with these paths show highly incoherent estimates even for paths crossing almost the same volumes. Therefore, our analysis and final interpretation is restricted to depths of 1 to 4 km: these analysis may provide hint on deeper structures once compared with other measurements.

3.2 P -wave attenuation tomography with the coda normalization method

The coda-normalization (CN) method has been first applied to the single-station estimate of the total S-wave inverse quality factor Q along the seismic path by Del Pezzo et al (2006) in the Mount Vesuvius volcanic area. The

single-path attenuation is obtained in a given frequency range with central frequency f_c by measuring the direct-S energy (E_k^s) and the coda-S energy in a time window centered around a given lapse time t_c ($E_k^c(f_c, t_c)$), and calculating their ratio. The single-path CN equation is:

$$\frac{1}{\pi f_c} \ln\left(\frac{E_k^s(f_c)}{E_k^c(f_c, t_c)}\right) = K(f_c, t_c, \theta, \phi) - \frac{2}{\pi f_c} \gamma \ln(r_k) - 2 \int_{r_k} \frac{dl}{v(l)Q(l)} \quad (1)$$

where r_k is the total length of the k^{th} ray, γ is the geometrical spreading, and $v(l)$ is the velocity of the medium measured along the ray-path. $K(f_c, t_c, \theta, \phi)$ takes into account the effect of the source radiation pattern, described by the take-off angle (θ) and azimuth (ϕ) and is the only other unknown variable (apart for Q) in the equation. As in given frequency bands diffraction effects, waveguides, and surface waves could affect the exponent γ of the geometrical spreading we choose to invert this parameter with the inverse average quality factor (La Rocca et al 2001; Morozov 2011; De Siena et al 2014).

As shown by Yoshimoto et al (1993) we can extend the CN method to the measurement of P -wave average attenuation (the P -wave quality factor, Q_p). We use active sources, that is, only P -waves are produced. We can reasonably assume a spherical source radiation pattern, hence, $K(f_c, t_c, \theta, \phi) = K(f_c, t_c)$, leaving Q_p as the only unknown in the inversion problem. We can thus apply the CN method to P -wave attenuation tomography under three assumptions:

- the small P - and S -wave mean free paths in the volcanic structures allow for a quick conversion of P -wave energy into coda energy,
- the seismic paths traveled by the waves producing the energy ratios filtered in the chosen frequency band can be approximated by a ray (curve),
- the lapse-time from origin is large enough to measure coda energy out of the P -wave transient regime.

The energy ratios vs. travel times behaviour reveal no evident anomalous energy-ratio increase localized in space at 6 Hz, indicative of anomalous coherent effects in the coda envelopes (De Siena et al 2014). As the lapse time t_c strongly influences the estimates of the average parameter if it is set to short lapse-times (Calvet and Margerin 2013) we set the start of the coda time-window of length 3 s to a lapse-time of 12 s. The P -energy time window is set to 1.5 s. The waveforms were selected depending on the coda-to-noise ratio (always larger than 1.5) at 6 Hz.

The final data-set is comprised of 20293 vertical seismic waveforms. The inversion of the energy ratios for the average parameters provides an average Q_p of 29: in the following we will discuss the variations with respect to the inverse of the average quality factor in the 3D space (ΔQ_p^{-1}), a direct measurement of attenuation. By considering these observations as well as the ideal distribution of our sources we invert the energy ratios for the attenuation parameters with the MuRAT code in a single-step inversion (De Siena et al 2014).

4 Synthetic tests

We want to discriminate the resolution we effectively achieve on a high attenuation anomaly in the center of the bay down to 4 km depth (Fig. 4). We start testing the resolution of the ΔQ_p^{-1} results assuming as input synthetic anomaly a high attenuation region in the centre of the island, roughly designed on the results of the velocity tomography (Figure 4, high attenuation correlated with high velocity). Hence, we impose a $8 \times 8 \times 4 \text{ km}^3$ volume of low quality factor under Port Foster. We generate synthetic P -to-coda energy ratios and we add Gaussian random error with zero mean and 3 times the standard deviation, equal to the 20% of the data value. We invert the synthetic data only in blocks crossed by at least 5 rays. We show the results on four horizontal slides at different depths (Fig. 4).

In order to test the resolution in the entire region we also perform a checkerboard test, whose output is shown on the same 4 horizontal slices used in Fig. 4 (Fig. 5, third column). We add the same amount of Gaussian random error to the synthetic P -to-coda energy ratios calculated from a checkerboard synthetic structure with 2 km node spacing, starting at 0 km, and having quality factors equals either to 100 or 1000. The checkerboard and synthetic anomaly test inputs and outputs are also shown on SN and WE vertical sections, crossing the inner bay (Fig. 3, dotted gray line).

The checkerboard test results are well resolved everywhere between depths of 1 and 3 km, while smearing affects the output at 4 km depth, especially in the regions contouring the island (Figs 5). The synthetic anomaly test is well resolved down to 4 km depth except for some smoothing on the southern and western sides of the images, between depths of 1 to 3 km (Figs 4 and 6). We conclude that we have good resolution in the volume under study. Also, a high attenuation anomaly, located in the center of the bay and as deep as 4 km, can be obtained by the inversion of real data.

5 Results and joint interpretation with the geological and geophysical results.

Fig. 5 shows 4 horizontal slices through the velocity and attenuation models down to a depth of 4 km (left-hand and central columns). Fig. 6b,c shows two vertical sections of these models, following the WE and SN directions as shown in Fig. 3 (gray dotted line). The P -wave percent velocity variations ($\% \Delta V_p$) are calculated by the P -wave velocity model of Zandomenighi et al (2009). The interpretation of our results is based on the analysis of the largest attenuation anomalies in the regions of major volcanological interest (Fig. 7).

In order to correlate the velocity and attenuation anomalies with those obtained by other geophysical and geological studies we discuss the results under the Oceanic Crust and caldera structure separately from the ones under the Port Foster. We also separate the discussion of the anomalies under Port

307 Foster bay in two different depth ranges (between depths of 1 and 2 km and
308 between depths of 3 and 4 km).

309 5.1 Oceanic Crust and caldera structure

310 No unique high-attenuation anomaly larger than 2 km is visible under the
311 Oceanic Crust contouring the island. An arc-shaped volume of small (2 km
312 average dimension) high-attenuation anomalies is located northeast of Decep-
313 tion at a depth of 1 km (Fig. 5). This volume, located in a low-velocity zone, is
314 partially visible in the 2 km tomograms. (Zandomeneghi et al 2009) interpret
315 the vast superficial low-velocity anomaly northeast of the island (1 to 2 km
316 depth, Fig. 5, left-hand column) as a zone of accumulation for sedimentary
317 materials and hydrothermal activity. From the depth extension and location
318 of the high-attenuation arc-shaped volume we confirm this interpretation, in
319 the sense that the high attenuation anomaly may actually locate the inner
320 boundary of the sedimentary structures and hydrothermal interactions.

321 Most of the source energy recorded near this boundary crosses the Port
322 Foster bay, that is, the most attenuating structure in the entire region (Vila
323 et al 1995; Martinez-Arevalo et al 2003). The fractured caldera as well as
324 the faults contouring the inner bay may also reflect or diffract direct energy.
325 Hence, we may not expect to image the exact lateral extension of these sedi-
326 ments: we may safely assume that velocity tomography provides more reliable
327 information on these structures.

328 Under the south-south-eastern part of the caldera structure, which consti-
329 tutes the part of Deception emerged out of the Ocean, we observe the largest
330 attenuation contrast, marking the entire depth range (e.g., Figs. 6c and 7 SN).
331 The low attenuation visible under the caldera defines an almost vertical bound-
332 ary with the high attenuation medium under Port Foster, in strong correlation
333 with the location of deep normal faults. The southern part of Deception is also
334 affected by large smearing (Fig. 6d), induced by the large velocity contrast af-
335 fecting the deep geometry of each source-station ray passing through it.

336 Pedrera et al (2012) obtain a vast conductive body extending SE of the Is-
337 land between depths of 2 and 12 km. The authors suggest emplacement of melt
338 in this volume driven by an ENE–WSW oriented and SSE dipping regional
339 normal fault. An almost vertical low-velocity and high-resistivity anomaly be-
340 tween depths of 2 and 6 km is located below Port Foster, connecting the vast
341 southeastern high-resistivity anomaly with the center of the island. The verti-
342 cal attenuation contrast is laterally disposed above the northwestern limit of
343 the deep high resistivity anomaly (Fig. 7).

344 Our results are compatible with previous studies (Ben-Zvi et al 2009; Zan-
345 domeneghi et al 2009; Pedrera et al 2012) affirming that the south-south-
346 eastern part of the Island may contain a certain volume of a fluid/melt which
347 may be the feeding path for the caldera. The section of this path, which should
348 be connected to the center of the island and present high attenuation, reduces
349 to our node spacing in the attenuation images at 4 km depth (Fig. 5, 4km).

350 Additionally, our results are also compatible with other interpretation
351 provided by Martí et al (2013) in which the deep feeding structures may simply
352 heat the upper crustal systems, where meteoric waters both penetrate and
353 circulate producing the high-attenuation anomaly in the centre of the caldera
354 (Fig. 7).

355 Deception faces the Bransfield Through from northwest (Martí et al 2013).
356 The collapsed part of its caldera structure corresponds to the northwestern
357 margin of the Through as well as to both steep almost-vertical normal faults
358 and strong attenuation contrasts (Fig. 7, upper-right panel). Velocity and re-
359 sistivity tomograms show clear low-velocity and high-resistivity connections of
360 the upper anomalies with deeper vast high-resistivity regions, extending south-
361 east of the island (Fig. 7, vertical section). Our results are in concordance with
362 those obtained by Pedrera et al (2012) which suggested that the feeding sys-
363 tem, through which fluids and melt materials either pass or heat the upper
364 crustal materials, starts south-east of the Island at around 6 km. The main
365 connection with the surface rises almost vertically towards the southeastern
366 margin of the Island (Zandomenighi et al 2009; Pedrera et al 2012), passing
367 through the high-attenuation contrasts southeast of the Island (Fig. 7). We
368 discuss in the next two sections if, how, and where the deep melt materials
369 are stored in the first 4 km under Deception.

370 5.2 From depths of 1 to 2 km under Port Foster

371 The Port Foster Bay (inner bay of Deception Island, Fig. 1) is dominated by
372 a large ΔQ_p^{-1} positive anomaly, that is, by high attenuation, down to a depth
373 of 2 km (Fig. 5, central column, red). In this depth range the high-attenuation
374 volume is contoured by average-to-low attenuation structures, mainly corre-
375 sponding to the exposed caldera rim (Figs. 5 and 6c). Zandomenighi et al
376 (2009) and Luzón et al (2011) both propose that unconsolidated volcanoclas-
377 tic and volcano-sedimentary materials, possibly producing high attenuation,
378 extend down to 1.2 - 1.4 km depth. We remark, that the anomaly in the cen-
379 tre of the bay shows much higher attenuation than the surroundings. This is
380 particularly relevant if we compare the results in the central bay with the arc
381 of high attenuation located northeast of the island, where low velocities are
382 also interpreted as induced by sediments (Zandomenighi et al 2009).

383 The strong P -wave attenuation is paired with a strong scattering signa-
384 ture (obtained by Prudencio et al (2013) under the bay) and suggests that
385 materials with higher attenuation capacity than sediments, like hydrothermal
386 interactions, intrude the first 2 km depth under the Port Foster bay. The top
387 of a resistivity anomaly obtained by Pedrera et al (2012) resembles pretty well
388 the low velocity and high attenuation structure under the bay at a depth of 2
389 km (Fig. 5, see also Zandomenighi et al (2009)).

390 Getting S -wave velocity information is important for the interpretation
391 of the attenuation anomalies. Luzón et al (2011) provide us information on
392 the transverse velocity wave-field between depths of 1 and 2 km. The lowest

393 S-wave velocities (related in the interpretation of Luzón et al (2011) to the
394 alterations produced by hydrothermal activity) are near Chilean station (Fig.
395 1) northeast of the bay. On the contrary, the largest velocities occur near the
396 SW caldera border, revealing the presence of compact materials at shallow
397 depths. The low velocity anomaly obtained by Luzón et al (2011) at 1 km
398 matches with the high-attenuation unique anomaly shifted towards the north
399 part of the bay.

400 De Siena et al (2010) depict zones of fluid accumulation coupled to a sur-
401 rounding network of normal faults beneath Pozzuoli (Campi Flegrei, Italy),
402 where the correlation of high attenuation and high V_p/V_s anomalies (Vanorio
403 et al 2005) is striking. This high attenuation anomaly is contoured by a hard
404 rock volume and associated with the caldera rim structure: this image is very
405 similar to the one we observe at Deception (compare our results with De Siena
406 et al (2010), Fig. 7c, markers X4, X5, and X6). In De Siena et al (2010) the
407 presence of melt is restricted to a small volume located at a depth of about
408 4 km embedded in a hard rock volume, and heating the geothermal system
409 under Pozzuoli.

410 The lateral extension of the high attenuation anomaly at Deception is
411 actually coincident with the bathymetry of the floor of the bay (Fig. 6a),
412 which reveals a broad uplift of the eastern side of the caldera (Cooper et al
413 1999). As proposed by Barclay et al (2009) bathymetric results could be caused
414 by sediment supply rates and hydrothermal alterations from the east of the
415 island or by a trap-door caldera deformation with its minimum subsidence in
416 the east. Both these causes are compatible with permeation of local meteoric
417 water and seawater in the intra-caldera formation.

418 Other additional evidences of the nature of sediment deposits, volcanoclas-
419 tic materials and hidrothermal alteration effects on the first 2 km shallow part
420 of the caldera floor, is obtained by the study of some geochemical aspects
421 of the area as the study of isotopes and noble gas data from fumarolic and
422 bubbling gases and hot spring waters (Kusakabe et al 2009). He and CO_2
423 are mainly of mantle origin, with no contribution of magmatic water to water
424 and gas samples, hot spring fluids being a mixture of local meteoric water
425 and seawater. Kusakabe et al (2009) infer that these results are due to the
426 existence of a heated hydrothermal system, with different temperatures in the
427 depth range between 1 and 2 km.

428 The shape of the high attenuation anomaly, contoured by the low-attenuation
429 caldera rim between depths of 1 and 2 km (Fig.s 5 and 6) is similar to the
430 one retrieved under different calderas and associated with the presence of hy-
431 drothermal alteration. The large low-velocity and high-attenuation structure
432 in the bay (Fig.s 5 and 6b,c) correlates well with high resistivity, high scat-
433 tering attenuation, and low S-wave velocities. Therefore, attenuation anomaly
434 shows a portion of the collapsed caldera center permeated by a geothermal
435 reservoirs, at least between depths of 1 and 2 km.

436 5.3 From depths of 3 to 4 km under Port Foster

437 Low velocity and high attenuation anomalies are less strong at depths larger
438 than 2 km under Port Foster (Fig.s 5 and 6). The percent velocity variations
439 show a continuous vertical anomaly between depths of 3 and 4 km, while the
440 high-attenuation anomaly is shaped as a spherical-like system having its basis
441 approximately at 3 km depth (Fig. 6b,c). No large unique high-attenuation
442 anomaly is visible at a depth of 4 km in the centre of the bay (Fig.s 5 and
443 6c). High-attenuation anomalies with lateral extensions of the order of our
444 node spacing connect the upper high attenuation semi-spherical anomaly with
445 depth. Our assumption is that seismic attenuation is more sensitive to the
446 presence of deep melt and fluids than seismic velocity, while velocity tomog-
447 raphy is able to sample larger depths (Hansen et al 2004; De Siena et al 2010;
448 Muksin et al 2013).

449 In their 2D and 3D resistivity maps Pedrera et al (2012) also reveal an
450 ENE–WSW elongated conductor located between 2 and 6 km depth beneath
451 the Port Foster bay, which they interpret as induced by a combination of
452 partial melt and hot fluids. The depth resolution of the magnetotelluric model,
453 which defines quite precisely the top of melt/fluid regions, is affected by the
454 resistivity of the superficial highly-resistive marine layers. This may cause an
455 incorrect depth definition of the highly resistive structures. As in attenuation
456 tomography we use ray-dependent measurements we assume we provide higher
457 resolution than in magnetotelluric imaging, again at the expense of depth
458 sampling.

459 The attenuation tomograms clearly show that the anomaly extends down
460 to a maximum depth of 3 km as a unique hemispherical body. The depth
461 extension and shape of the high attenuation anomaly at depths of 3 to 4 km is
462 similar to the ones observed in other areas, e.g., by De Siena et al (2010) in the
463 Campi Flegrei caldera, by Muksin et al (2013) in the Tarutung Basin, and by
464 Bohm et al (2013) in the Kendeng Basin. These observations are always related
465 to sedimentary or volcanoclastic deposits overlying active geothermal and gas
466 reservoirs. However, other studies, interpret this high attenuation anomaly and
467 low velocity body as the presence of shallow partial melted magma body such
468 as Koulakov et al (2009) and Jaxybulatov et al (2014) in Toba caldera or
469 Ohlendorf et al (2014) in Okmok Volcano. In Okmok volcano the authors
470 found the same pattern of velocity and attenuation observed in Deception
471 Island and they interpreted the shallow part of the anomaly (surface to 2 km)
472 as caldera fill, groundwater and small pods of magma and the deeper part of
473 the anomaly (from 4 to 6 km) as a magma storage zone. This geodynamic
474 model is compatible with the subduction processes or slab rollback suggested
475 by Maestro et al (2007).

476 As indicated previously in section 2 and above, our results are compatible
477 with both proposed models. The modelled volume of melted rocks of Ben-Zvi
478 et al (2009) (less than $15 - 20 km^3$) in depth can coexist with other effects
479 as a network of magma and fluid filled batches of size either lower than or
480 equal to our resolution seems the more reliable explanation for the absence

481 of a unique high attenuation anomaly down to 4 km. This network could be
482 visible as a unique velocity and conductive anomaly, which may provide the
483 main heat source that sustains the geothermal system in the first 3 km of the
484 crust (Martí et al 2013).

485 6 Conclusions

486 In the present work we obtain the 3D P-wave attenuation model of Deception
487 Island by using coda normalization method. The methodology used in this
488 study is stable, robust and reliable. The reliability of the method is based on
489 the similarity of results with other studies. The study of S-waves and V_p/V_s
490 distribution might better constrain the inner structure of the island.

491 We have provided new results showing the complex attenuative structure of
492 the island with the presence of bodies of low and high attenuation. As in the
493 velocity tomography, we find a limitation in the range of depth that we are
494 able to solve due to the structure of the thinned oceanic crust region where
495 the Moho is 4-5 km depth and it implies a physical barrier.

496 One of the most important remarks is the presence of high attenuation body
497 in the center of the island which extends from the surface to our resolution
498 limit. The interpretation of this anomaly in the first two kilometers agrees
499 almost all researchers who have worked on the island and is associated with the
500 effects of sedimentary and volcanoclastic deposits, hydrothermal interactions
501 and highly fractured material.

502 The interpretation of the deeper structure is more complex, mainly due
503 to the lack of S-waves data. Thus, our results are consistent with two pos-
504 sible models. In the first, the high attenuation and low velocity is due to a
505 hydrothermal system effects. On the other, this anomaly is interpreted as the
506 existence of a partially molten magmatic body. A combination of these two
507 models is also compatible with our results. It will be necessary to continue
508 working to incorporate data from S waves or other methodologies to give light
509 to the interpretations.

510 7 Fig. captions

511 **Fig. 1:** Regional setting and location of Deception Island in the South Shetland
512 Islands archipelago, Antarctica (upper two panels). Bottom panel: Toponyms
513 (bold italics), historical eruption sites (white on black rectangle), and research
514 stations active or destroyed by the recent eruptions (regular bold), are shown
515 on the contour map of Deception Island.

516 **Fig. 2:** The vertical records of a seismic shot produced on the 8 of January
517 2005, located in the center of the Port Foster Bay (blue star), and recorded at
518 four seismic land stations (M, F, J, H). The gray dotted line crossing near the
519 center of the bay indicate the location and direction of the vertical sections

shown in Fig. (6). The panels on the right show the signal spectrum (S, blue lines) and noise spectrum (N, red lines) for each recording.

Fig. 3: Configuration of the TOMODEC seismic tomography experiment. a) Land and ocean bottom seismometers (red triangles) and shots locations (gray lines) are drawn on a contour map of the island. In the top-right panel we a zoom on the center of the island (Port Foster bay). b): 3D and 2D source-station ray-paths obtained by using a Thurber-modified ray-bending approach. All the events are approximately located at 0 km depth and produced by air-guns. The red contour map imposed on the rays shows the location and shape of Deception Island with respect to the experiment setting.

Fig. 4: Upper panel: The synthetic anomaly test input is designed to show the reproducibility of a simplified deep high-attenuation anomaly under the Port Foster bay. The high attenuation anomaly has a dimension of $8 \times 8 \times 4 \text{ km}^3$ and is characterized by a quality factor of 3. Lower panels: four horizontal slices through the output of the synthetic anomaly test taken at different depths with respect to the sea level. The ΔQ_p^{-1} grey scale shows the variations with respect to the average quality factor.

Fig. 5: The results of velocity tomography (Zandomeneghi et al 2009, left-hand column), of the attenuation tomography (central column) and the output of the checkerboard test (right-hand column) are shown on four horizontal slices taken at different depths. The left-hand color scale shows the percent variations of the velocity model with respect to its average. Both the central color scale and the right-hand grayscale show the variations of the attenuation model with respect to the average quality factor. The contour of Deception Island is over-imposed on each panel.

Fig. 6: Bathymetry (a), velocity model (Zandomeneghi et al 2009, b), attenuation model (c), and the synthetic tests (d) are all shown on two vertical sections crossing the Island (gray dotted lines in Fig. 3). The vertical scale in the velocity and attenuation images is enlarged for clarity. b) The color scale shows the percent variations of the velocity model with respect to its average. c) The color scale shows the variations of the attenuation model with respect to the average quality factor. d) The ΔQ_p^{-1} grey scale shows the variations with respect to the average quality factor. The inputs are shown above the corresponding outputs for both the checkerboard test and the synthetic anomaly test. The input of the synthetic anomaly test is described in the caption of Fig. 4.

Fig. 7: Schematic interpretation of the attenuation model, carried out with reference to the 3D velocity (Zandomeneghi et al 2009) and resistivity (Pedrera et al 2012) models, and constrained by other geophysical, geological, and geochemical observations, as described in the text. In the upper-right panel we show a horizontal section of the region taken at 8 km depth and depicting the portion of the Bransfield Through as well as the horizontal contour of the high resistivity anomaly contained in the region under study. We also infer from our analysis both meteoric water circulation in the upper crust and heat rising towards surface. We depict the depth dependence of the anomalies described in the text on two vertical sections, taken between depths of 0 and

566 10 km and crossing the Island (gray dotted lines in Fig. 3). Below a depth of
567 4 km the sketch is based on the 3D velocity and resistivity results only. Below
568 5.5 km the sketch is based on the resistivity model only.

569 **Acknowledgements** We gratefully acknowledge editor Dr Rycroft, Prof. Martí and one
570 anonymous reviewer whose useful suggestions greatly improved the manuscript. This work
571 has been partially supported by the Spanish project Ephestos, CGL2011-29499-C02-01; by
572 the EU project EC-FP7 MEDiterranean SUPersite Volcanoes (MED-SUV); by the Basque
573 Government researcher training program BFI09.277 and by the Regional project ‘Grupo de
574 Investigacin en Geofísica y Sismología de la Junta de Andalucía, RNM104’. Edoardo del Pezzo
575 has been partly supported by DPC-INGV projects UNREST, SPEED and V2 (Precursori).
576 We also thank Christine Thomas, Ralf Hetzel, and Stephan Klemme for the important
577 suggestions regarding both the method and the interpretation.

578 References

- 579 Aki K, Richards P (1980) Quantitative Seismology - Theory and Methods. W. H. Freeman,
580 San Francisco
- 581 Almendros J, Ibez J, Alguacil G, Del Pezzo E, Ortiz R (1997) Array tracking of the volcanic
582 tremor source at Deception Island, Antarctica. *Geophysical Research Letters* 24:3069–
583 3072
- 584 Barclay A, Wilcock WSD, Ibáñez J (2009) Bathymetric constraints on the tectonic and vol-
585 canic evolution of Deception Island Volcano, South Shetland Islands. *Antarctic Science*
586 21:153–167
- 587 Ben-Zvi T, Wilcock WSD, Barclay A, Zandomenighi D, Ibáñez J, Almendros J (2009) The
588 P wave velocity structure of Deception Island, Antarctica, from two dimensional seismic
589 tomography. *Journal of Volcanology and Geothermal Research* 180:67–80
- 590 Benitez MC, Ramirez J, Segura JC, Ibez J, Almendros J, Garca-Yeguas A, Corts G (2007)
591 Continuous hmm-bases seismic-event classification at Deception Island, Antarctica. *Geo-
592 science and Remote Sensing, IEEE Transactions* 45:138–146
- 593 Berrococo M, Prates G, Fernández-Ros A, Garca A (2012) Normal vector analysis from
594 gnss-gps data applied to Deception volcano surface deformation. *Geophysical Journal
595 International* 190:1562–1570
- 596 Bohm M, Haberland C, Asch G (2013) Imaging fluid-related subduction processes be-
597 neath Central Java (Indonesia) using seismic attenuation tomography. *Tectonophysics*
598 590:175–188
- 599 Calvet M, Margerin L (2013) Spatial variations of seismic attenuation in the Pyrenees:
600 coda Q and peak delay time analysis. *Bulletin of Seismological Society of America*
601 103:doi:10.1785/0120120,239
- 602 Carmona E, Almendros J, Pea JA, Ibáñez JM (2010) Characterization of fracture systems
603 using precise array locations of earthquake multiplets: An example at Deception Island
604 volcano, Antarctica. *Journal of Geophysical Research: Solid Earth* 115
- 605 Carmona E, Almendros J, Serrano I, Stich D, Ibáñez J (2012) Results of seismic monitoring
606 surveys of Deception Island volcano, from 1999-2011. *Antarctic Science* 24:485–499
- 607 Carmona E, Almendros J, Martín R, Corts G, Alguacil G, Moreno J, Martín JB, Martos A,
608 Serrano D, Stich, Ibez J (2014) Advances in seismic monitoring at Deception Island
609 volcano (Antarctica) since the international polar year. *Annals of Geophysics* 57
- 610 Caselli A, Santos-Alfonso M, Augusto MR (2004) Gases fumarólicos de la isla Decepción
611 (Shetland del Sur, Antártida): Variaciones químicas y depósitos vinculados a la crisis
612 sísmica de 1999. *Asociación Geológica Argentina Revista* 59:291–302
- 613 Caselli A, Badi G, Bonatto AL, Bengoa CL, Augusto MR, Bidone A, Ibáñez J (2007) Ac-
614 tividad sísmica y composición química fumarólica anómala debido a posible efecto sello
615 en el sistema volcánico, Isla Decepción (Antártida). *Revista de la Asociación Geológica
616 Argentina* 62:545–552

- 617 Catalan M, Agudo LM, Muoz-Martin A (2006) Geomagnetic secular variations of Bransfield
618 Strait (Western Antarctica) from analysis of marine crossover data. *Geophysical Journal*
619 *International* 165:73–86
- 620 Chouet B (2003) Volcano seismology. *PAGEOPH* 160:739–788
- 621 Cooper AP, Smellie JL, Maylin J (1999) Evidence for shallowing and uplift from bathymetric
622 records of Deception Island, Antarctica. *Antarctic Science* 10:455–461
- 623 De Siena L, Del Pezzo E, Bianco F, Tramelli A (2009) Multiple resolution seismic attenuation
624 imaging at Mt. Vesuvius. *Physics of the Earth and Planetary Interiors* 173:17–32
- 625 De Siena L, Del Pezzo E, Bianco F (2010) Seismic attenuation imaging of Campi Flegrei:
626 Evidence of gas reservoirs, hydrothermal basins and feeding systems. *Journal of Geo-*
627 *physical Research* 115
- 628 De Siena L, Del Pezzo E, Thomas C, Curtis A, Margerin L (2013) Seismic energy envelopes
629 in volcanic media: in need of boundary conditions. *Geophysical Journal International*
630 195 (2):1102–1119
- 631 De Siena L, Thomas C, Aster R (2014) Multi-scale reasonable attenuation tomography
632 analysis (MuRAT): an imaging algorithm designed for volcanic regions. *Journal of Vol-*
633 *canology and Geothermal Research* 277:22–35
- 634 Del Pezzo E (2008) Seismic wave scattering in volcanoes. *Advances in Geophysics* 50:353–371
- 635 Del Pezzo E, Bianco F, De Siena L, Zollo A (2006) Small scale shallow attenuation structure
636 at Mt. Vesuvius. *Physics of the Earth and Planetary Interiors* 157:257–268
- 637 Eberhart-Phillips D, Reyners M, Chadwick M, Stuart G (2008) Three-dimensional atten-
638 uation structure of the Hikurangi subduction zone in the central North Island, New
639 Zealand. *Geophysical Journal International* 174:418–434
- 640 Fernández-Ibáñez F, Pérez-López R, Martínez-Díaz JJ, Paredes C, Giner-Robles J, Caselli
641 A, Ibáñez J (2005) Costa Recta Beach, Deception Island, West Antarctica: a retreated
642 scarp of a submarine fault. *Antarctic Science* 17:418–426
- 643 García-Yeguas A, Almendros J, Abella R, Ibáñez J (2010) Quantitative analysis of seismic
644 wave propagation anomalies in azimuth and apparent slowness at Deception Island
645 volcano (Antarctica) using seismic arrays. *Geophysical Journal International* pp doi:
646 10.1111/j.1365-246X.2010.04,864.x
- 647 Haberland C, Rietbrock A (2001) Attenuation tomography in the western central Andes: A
648 detailed insight into the structure of a magmatic arc. *Journal of Geophysical Research*
649 106(B6):11,151–11,167
- 650 Hansen S, Thurber CH, Mandernach M, Haslinger F, Doran C (2004) Seismic Velocity
651 and Attenuation Structure of the East Rift Zone and South Flank of Kilauea Volcano,
652 Hawaii. *Bulletin of the Seismological Society of America* 94:1430–1440
- 653 Hunsen S, Smith RB, Waite GP (2004) Evidence for gas and magmatic sources beneath
654 Yellowstone volcanic field from seismic tomographic imaging. *Journal of Volcanology*
655 *and Geothermal Research* 131:397–410
- 656 Ibáñez J, Almendros J, Alguacil G, Morales J, Del Pezzo E, Ortiz R (1997) Eventos ssmicos
657 de largo periodo en la isla decepcin: evidencias de una zona volcnica activa. *Boletn de*
658 *la RSEHN* 93:103–110
- 659 Ibáñez J, Del Pezzo E, Morales J, Alguacil G, Almendros J, Ortiz R, La Rocca M, García
660 A (2000) Seismovolcanic signals at Deception Island Volcano, Antarctica: wave field
661 analysis and source modelling. *Journal of Geophysical Research* 135:13,905–13,931
- 662 Ibáñez J, Carmona E, Almendros J, Saccorotti G, Del Pezzo E, Abril M, Ortiz R (2003) The
663 1998-1999 seismic series at deception island volcano, antarctica. *Journal of Volcanology*
664 *and Geothermal Research* 128:65–88
- 665 Jaxybulatov K, Shapiro NM, Koulakov I, Mordret A, Lands M, Sens-Schonfelder C (2014)
666 A large magmatic sill complex beneath the toba caldera. *Science* 346:617–619
- 667 Julian BR, Ross A, Foulger GR, Evans JR (1996) Three-dimensional seismic image of a
668 geothermal reservoir: the Geysers, California. *Geophysical Research Letters* 23:685–688
- 669 Julian BR, Pitt A, Foulger GR (1998) Seismic image of CO2 reservoir beneath a seismically
670 active volcano. *Geophysical Journal International* 133:F7–F10
- 671 Koulakov I, Yudistira T, Luehr BG (2009) P, s velocity and vp/vs ratio beneath the toba
672 caldera complex (northern sumatra) from local earthquake tomography. *Geophysical*
673 *Journal International* 117(3):1121–1139

- 674 Koulakov I, Bindi D, Parolai S, Grosser H, Milkereit C (2010) Distribution of Seismic Ve-
675 locities and Attenuation in the Crust Beneath the North Anatolian Fault (Turkey)
676 from Local Earthquake Tomography. *Bulletin of the Seismological Society of America*
677 100(1):207–224
- 678 Kusakabe M, Nagao K, Ohba T, Hun Seo J, Park S, Lee J, Park B (2009) Noble gas and
679 stable isotope geochemistry of the thermal fluids from Deception Island, Antarctica.
680 *Antarctic Science* 21:255–267
- 681 Kuznetsov P, Koulakov I (2014) The three-dimensional structure beneath the Popocatepetl
682 volcano (Mexico) based on local earthquake seismic tomography. *Journal of Volcanology*
683 and *Geothermal Research* 276:10–21
- 684 La Rocca M, Del Pezzo E, Simini M, Scarpa R, De Luca G (2001) Array analysis of seis-
685 mograms for explosive sources: evidence for surface waves scattered at the main topo-
686 graphical features. *Bulletin of the Seismological Society of America* 91:219–231
- 687 Lees JM, Lindley GT (1994) Three-dimensional Attenuation Tomography at Loma Prieta:
688 Inverting t^* for Q . *Journal of Geophysical Research* 99(B4):6843–6863
- 689 Luzón F, Almendros J, García-Jerez A (2011) Shallow structure of Deception Island, Antarc-
690 tica, from correlations of ambient noise on a set of dense seismic arrays. *Geophysical*
691 *Journal International* 185:737–748
- 692 Maestro A, Somoza L, Rey J, Martínez-Fras J, López-Martínez J (2007) Active tectonics, fault
693 patterns and stress field of deception island: a response to oblique convergence between
694 the Pacific and Antarctic plates. *Journal of South American Earth Sciences* 23:256–268
- 695 Martí J, Vila J, Rey J (1996) Deception island (Bransfield Strait, Antarctica): an example of
696 a volcanic caldera development by extensional tectonics. McGuire, W J, Jones, A P and
697 Neuberg, J, eds *Volcano instability on the Earth and other planets Special Publication*
698 of the Geological Society, London 110:253–265
- 699 Martí J, Geyer A, Aguirre-Díaz G (2013) Origin and evolution of the Deception Island
700 caldera (South Shetland Islands, Antarctica). *Bulletin of Volcanology* 75:732–750
- 701 Muñoz Martín A, Catalan M, Martín J, Carbo A (2005) Upper structure of Deception Island
702 area (Bransfield Strait, Antarctica) from gravity and magnetic modelling. *Antarctic*
703 *Science* 17:213–224
- 704 Martínez-Arevalo C, Bianco F, Ibáñez J, Del Pezzo E (2003) Shallow seismic attenuation and
705 shear-wave splitting in the short-period range of Deception Island volcano (Antarctica).
706 *Journal of Volcanology and Geothermal Research* 128:89–113
- 707 Matsumoto S, Uehira K, Watanabe A, Goto K, Iio Y, Hirata N, Okada T, Takahashi H,
708 Shimizu H, Shinohara M, Kanazawa T (2009) High resolution Q^{-1} estimation based
709 on extension of coda normalization method and its application to P-wave attenuation
710 structure in the aftershock area of the 2005 West Off Fukuoka Prefecture Earthquake
711 (M 7.0). *Geophysical Journal International* 179:1039–1054
- 712 Melo R, Vieira G, Caselli A, Ramos M (2012) Susceptibility modelling of hummocky terrain
713 distribution using the information value method (Deception Island, Antarctic Penin-
714 sula). *Geomorphology* 155-156:88–95
- 715 Morozov IB (2011) Mechanisms of geometrical seismic attenuation. *Annals of Geophysics*
716 54(3)
- 717 Muksin U, Haberland C, Bauer K, Weber M (2013) Three-dimensional upper crustal
718 structure of the geothermal system in Tarutung (North Sumatra, Indonesia) re-
719 vealed by seismic attenuation tomography. *Geophysical Journal International* 195, doi:
720 10.1093/gji/ggt383:2037–2049
- 721 Ohlendorf SJ, Thurber C, Pesicek JD, Prejean SG (2014) Seismicity and seismic structure at
722 Okmok volcano, Alaska. *Journal of Volcanology and Geothermal Research* 278:103–119
- 723 Ortiz R, García A, Aparicio A, Blanco I, Felpeto A, Del Rey R, Villegas MT, Ibáñez J,
724 Morales J, Del Pezzo E, Olmedillas J, Astiz MM, Vila J, Ramos M, Viramonte JG,
725 Risso C, Caselli A (1997) Monitoring of the volcanic activity of Deception Island, south
726 Shetland Islands, Antarctica (1986–1995). In: Ricci, CA (Ed) *The Antarctic Region: Ge-*
727 *ological Evolution and Processes*, Terra Antarctica Publications, Siena pp pp. 1071–1076
- 728 Pedrera A, Ruíz-Constán A, Heredia N, Galindo-Zaldívar J, Bohoyo F, Marín-Lechado C,
729 Ruano P, Somoza L (2012) The fracture system and the melt emplacement beneath the
730 Deception Island active volcano, South Shetland Islands, Antarctica. *Antarctic Science*
731 24:173–182

- 732 Prates G, Berrocoso M, Fernández-Ros A, Garca A (2013) Enhancement of sub-daily position-
733 ing solutions for surface deformation monitoring at deception volcano (south shetland
734 islands, antarctica). *Bulletin of Volcanology* 75:1–10
- 735 Priyono A, Suantika G, Widiyantoro S, Nugraba AD (2011) Three-dimensiona seismic at-
736 tenuation structure of Mt. Guntur, West Java, Indonesia. *International Journal of To-
737 mography and Simulation* 17:17–28
- 738 Prudencio J, Ibáñez J, García-Yeguas A, Del Pezzo E (2013) Spatial distribution of intrinsic
739 and scattering seismic attenuation in active volcanic islands, II: Deception island images.
740 *Geophysical Journal International* 195 (3):1957–1969, doi: 10.1093/gji/ggt360
- 741 Saccorotti G, Almendros J, Carmona E, Ibáñez J, Del Pezzo E (2001) Slowness Anoma-
742 lies from two dense seismic arrays at Deception Island volcano, Antarctica. *Bulletin of
743 Seismological Society of America* 91:561–571
- 744 Sato H, Fehler MC, Maeda T (2012) *Seismic Wave Propagation and Scattering in the het-
745 erogeneous Earth: Second Edition*. Springer, New York, USA
- 746 Schurr B, Asch G, Rietbrock A, Trumbull R, Haberland CH (2003) Complex patterns of
747 fluid and melt transport in the central Andean subduction zone revealed by attenuation
748 tomography. *Earth and Planetary Science Letters* 215:105–119
- 749 Smellie JL (2001) Lithostratigraphy and volcanic evolution of deception island, south shetland
750 islands. *Antarctic Science* 13:118–209
- 751 Smellie JL, López-Martínez J, Headland RK, Hernández-Cifuentes F, Maestro A, Millar
752 IL, Thomson JW (2002) *Geology and geomorphology of Deception Island*. Cambridge,
753 British Antarctic Survey, p 77p
- 754 Takanami T, Selwyn Sacks I, Hasegawa A (2000) Attenuation structure beneath the volcanic
755 front in northeastern Japan from broad-band seismograms. *Physics of the Earth and
756 Planetary Interior* 121:339–357
- 757 Tejedo P, Gutierrez B, Pertierra LR, Benayas J (2014) Analysis of published scienti-
758 fic research from deception island, south shetland islands. *Antarctic Science* p
759 doi:10.1017/S0954102014000455
- 760 Torrecillas C, Berrocoso M, Pérez-López R, Torrecillas M (2012) Determination of volumet-
761 ric variations and coastal changes due to historical volcanic eruptions using historical
762 maps and remote-sensing at Deception Island (West-Antarctica). *Geomorphology* 136:6–
763 14
- 764 Torrecillas C, Berrocoso M, Felpeto A, Torrecillas M, García A (2013) Reconstructing
765 palaeo-volcanic geometries using a Geodynamic Regression Model (GRM): Applica-
766 tion to Deception Island Volcano (South Shetland Islands, Antarctica). *Geomorphology*
767 182:79–88
- 768 Vanorio T, Virieux J, Capuano P, Russo G (2005) Three-dimensional tomogra-
769 phy from P wave and S wave microearthquake travel times and rock physics
770 characterization of the Campi Flegrei Caldera. *Journal of Geophysical Research*
771 110(B03201):doi:10.129/2004JB003,102
- 772 Vila J, Martí J, Ortiz R, García A, Correig AM (1992) Volcanic tremors at deception island,
773 south shetland islands, antarctica. *Journal of Volcanology and Geothermal Research*
774 53:1–4
- 775 Vila J, Correig AM, Martí J (1995) Attenuation source parameters at Deception Island
776 (South Shetland Islands, Antarctica). *Pure and Applied Geophysics* 144:229–250
- 777 Yoshimoto K, Sato H, Ohtake M (1993) Frequency-dependent attenuation of P and S waves
778 in Kanto area, Japan, based on the coda-normalization method. *Geophysical Journal
779 International* 114:165–174
- 780 Zandomenighi D, Barclay A, Almendros J, Ibáñez J, Wilcock WSD (2009) Crustal structure
781 of Deception Island volcano from P-wave seismic tomography: tectonic and volcanic
782 implications. *Journal of Geophysical Research* 114

Surveys in Geophysics manuscript No. (will be inserted by the editor)

The 3D attenuation structure of Deception Island (Antarctica)

**J. Prudencio · L. De Siena · J.
M. Ibáñez · E. Del Pezzo · A.
García-Yeguas · A. Díaz-Moreno**

Received: date / Accepted: date

J. Prudencio

Instituto Andaluz de Geofísica, University of Granada, Profesor Clavera 12, 18071 Granada, Spain

Dept. Física Teórica y del Cosmos, University of Granada, Fuentenueva S/N, 18001 Granada, Spain

INVOLCAN, Antiguo Hotel Taoro, Parque Taoro 22, 38400 Puerto de la Cruz, Tenerife, Spain

E-mail: janire@ugr.es

L. De Siena

University of Münster, Institut für Geophysik, Correnstrasse 24, Münster, 48149, Germany.

University of Aberdeen, School of Geosciences, Geology and Petroleum Geology, Meston Building, King's College, Aberdeen AB24 3UE Scotland

Tel. +492518334725

Fax +492518336100

E-mail: lucadesiena@uni-muenster.de

J. M. Ibáñez

Instituto Andaluz de Geofísica, University of Granada, Profesor Clavera 12, 18071 Granada, Spain

Dept. Física Teórica y del Cosmos, University of Granada, Fuentenueva S/N, 18001 Granada, Spain

Istituto Nazionale di Geofisica e Vulcanologia, Sezione di Catania -Osservatorio Etneo, 95125 Catania, Italy

E. Del Pezzo

Istituto Nazionale di Geofisica e Vulcanologia, Sezione di Napoli -Osservatorio Vesuviano, Via Diocleziano 328, 80124 Naples, Italy

Instituto Andaluz de Geofísica, University of Granada, Profesor Clavera 12, 18071 Granada, Spain

A. García-Yeguas

Dept. Física Aplicada, University of Cádiz, Av. Duque de Nájera 18, 11002, Cádiz, Spain

Instituto Andaluz de Geofísica, University of Granada, Profesor Clavera 12, 18071 Granada, Spain

INVOLCAN, Antiguo Hotel Taoro, Parque Taoro 22, 38400 Puerto de la Cruz, Tenerife, Spain

Abstract The seismic and volcanological structure of Deception Island (Antarctica) is an intense focus topic in Volcano Geophysics. The interpretations given by scientists on the origin, nature, and location of the structures buried under the island strongly diverge. We present a high-resolution 3D P -wave attenuation tomography model obtained by using the coda normalization method on 20,293 high-quality waveforms produced by active sources. The checkerboard and synthetic anomaly tests guarantee the reproduction of the input anomalies under the island down to a depth of 4 km. The results, once compared with our current knowledge on the geological, geochemical, and geophysical structure of the region, depict Deception as a ~~broken-collapsed calderic structure~~ **piecemeal caldera structure** leant out of the Bransfield Trough. High attenuation anomalies contouring the north-eastern emerged caldera rim correlate with the locations of sediments. In our interpretation, the main attenuation contrast, which appears under the collapsed southeastern caldera rim, is related to the deeper feeding systems. A unique P -wave high attenuation spherical-like anomaly in the inner bay extends between depths of 1 and 3 km. The northern contour of the anomaly coincides with the calderic rim both at 1 and 2 km, while smaller anomalies connect it with deeper structures below 3 km, dipping towards the Bransfield Trough. In our interpretation, the large upper anomaly is caused by a high-temperature shallow (1 to 3 km deep) geothermal system, located beneath the sediment-filled bay in the ~~cracked-collapsed caldera center~~ **collapsed blocks**, and heated by smaller, deeper contributions of molten materials (magma) rising from southeast.

Keywords Attenuation · Scattering · Tomography · Antarctica

1 Introduction

Deception Island (Fig. 1) ~~can be~~ **is** considered as a laboratory for Volcano Geophysics due to the large number of multidisciplinary studies focused both on imaging its surface and deep structures and on monitoring its volcanic activity. ~~Scientists have widely studied the origin and morphology of Deception Island, bringing formed general and local models (e.g. Martí et al 1996, 2013; Smellie et al 2002; Fernández-Ibáñez et al 2005; Maestro et al 2007; Barclay et al 2009; Melo et al 2012; Torrecillas et al 2012, 2013). The study of the seismic activity of the volcano is probably the most active and productive research line, as reported by Tejedo et al (2014). There are many results that help to better understand the dynamic and volcanological framework of the area as Vila et al (1992), Almendros et al (1997), Ibáñez et al (1997), Ibáñez et al~~

A. Díaz-Moreno

Instituto Andaluz de Geofísica, University of Granada, Profesor Clavera 12, 18071 Granada, Spain

Dept. Física Teórica y del Cosmos, University of Granada, Fuentenueva S/N, 18001 Granada, Spain

INVOLCAN, Antiguo Hotel Taoro, Parque Taoro 22, 38400 Puerto de la Cruz, Tenerife, Spain

(2000), Ibáñez et al (2003), Saccorotti et al (2001), Martínez-Arevalo et al (2003), Benitez et al (2007), Carmona et al (2010), Carmona et al (2012), Carmona et al (2014) and García-Yeguas et al (2010). and seismic activity of the island. The velocity, attenuation, and magnetotelluric structures have been obtained by using passive and active data. One of the objectives of these seismic studies is to provide 2- or 3-D structure of the area, by using active or passive data as has been done by (Ben-Zvi et al 2009; Zandomenighi et al 2009; Prudencio et al 2013). These seismic models have been used to confirm or help to built other geophysical or geodynamic models of the island, as magnetotelluric (Pedrera et al 2012), geomagnetic (Muñoz Martín et al 2005), gravimetric (Catalan et al 2006) or geodetic (Berrocoso et al 2012; Prates et al 2013). as well as Additionally, geochemical analysis as the composition and ratio of stable isotopes and gasses produced by fumaroles (Caselli et al 2004, 2007; Kusakabe et al 2009) are also very well know, and provide exact important information on the presence and origin of magma and fluids. All these efforts still fail in creating a unique shared structural and dynamic model of the island, with particular debate on its deep volcanic structure (Martí et al 2013; Torrecillas et al 2013). This debate focuses on the presence and location either of a fractured geothermal system or a shallow, active magma chamber beneath the sediment filled bay in the center of the volcanic island as well as on its connections with deeper structures. Nowadays with these observables the research community is working to provide a geodynamic and volcanological model that could unify all of them in a single interpretation as those done by (Smellie 2001; Martí et al 2013; Berrocoso et al 2012; Pedrera et al 2012).

The imaging of region-specific velocity and attenuation through direct-wave tomography provides striking results at local, regional, and global scales (e.g., Schurr et al 2003 and Eberhart-Phillips et al 2008). Attenuation tomography is today a standard technique and several codes include this important measurement in their tomographic algorithms (Lees and Lindley 1994; Schurr et al 2003; Hansen et al 2004; Eberhart-Phillips et al 2008; Koulakov et al 2010). Due to the higher sensitivity of the attenuation parameters to the presence of fluids and melt with respect to velocity, attenuation tomography may provide decisive data to discriminate the location and nature of the volcanic and seismic structures under Deception Island.

The modeling of energy (amplitude) propagation in highly-heterogeneous local-scale volcanic media is especially complicated by frequency-dependent source and site effects. In these media, scattering phenomena produce high-frequency long wave-trains of incoherent radiation (coda waves, e.g., Sato et al 2012), affected by dispersion as well as by interference, diffraction, and resonant effects. The coherency in the corresponding direct signals is also quickly lost (La Rocca et al 2001; Chouet 2003; De Siena et al 2013). In these media, we may retrieve P - and S -wave attenuation parameters independently of the site and instrumental transfer functions by using the coda-normalization method (Aki and Richards 1980; Yoshimoto et al 1993; Sato et al 2012). In recent years, this method has been applied to S -wave attenuation tomography at local scale, exploiting the strong scattering effects produced by strong het-

59 erogeneity in volcanic regions (Del Pezzo et al 2006; Matsumoto et al 2009;
60 Sato et al 2012; De Siena et al 2010).

61 The coda-normalization method is based on the equation that correlates
62 the ratio between the S-wave direct energy and the coda-wave energy to the
63 spatial distribution of the inverse total quality factors calculated along the
64 source-station ray-path (Del Pezzo et al 2006; De Siena et al 2009, 2014).
65 If active sources are available, the spatial distribution of P -wave attenuation
66 becomes the only unknown if the final coda-normalization inverse problem,
67 that is, the method may be exploited at best.

68 In this study, we obtain the P -wave total quality factor (Q_p), which mea-
69 sures the anelastic and scattering losses suffered by P -waves while propagating
70 into the medium. This quantity provides information on the physical, chemical,
71 and geological state of the Earth, and becomes especially useful if compared
72 with seismic velocities. A wide range of physical properties must be consid-
73 ered before discussing the joint results of velocity and attenuation tomography.
74 Their combined interpretation is a decisive tool in discriminating volumes ei-
75 ther permeated by fluids or characterized by structural discontinuities (Schurr
76 et al 2003; Eberhart-Phillips et al 2008; De Siena et al 2010).

77 The relation between velocity and attenuation is often ambiguous. High
78 attenuation and low velocity do not always mean the presence of melt in vol-
79 canoes, as fluids, gasses, faults, and, more generally, unconsolidated materials
80 (like sediments) all produce high attenuation in the presence of different veloc-
81 ity signatures (Haberland and Rietbrock 2001; Schurr et al 2003; Hansen et al
82 2004; De Siena et al 2010; Muksin et al 2013). Several authors (e.g., Priyono
83 et al 2011) suggest that high ΔQ_p^{-1} and low ΔV_p^{-1} in volcanic regions are
84 related to a magmatic system, while others (e.g., Takanami et al 2000) relate
85 these correlation to high-temperature zones without partial melting.

86 The P -to- S velocity ratio (V_p/V_s) is a decisive parameter to discriminate
87 magma from either fluids or gasses if spatially correlated with high attenuation
88 (Hansen et al 2004; Vanorio et al 2005; De Siena et al 2010; Kuznetsov and
89 Koulakov 2014). Low V_p/V_s anomalies and high attenuation may in fact be
90 associated with the presence of gas filling faults and fractures, hydrothermal
91 basins, and CO_2 emission beneath volcanoes, mountain ranges, and geothermal
92 reservoirs (Julian et al 1996, 1998; Hunsen et al 2004; Hansen et al 2004). The
93 correlation of high V_p/V_s with high attenuation is critical to discriminate fluids
94 from melt. As no V_p/V_s ratio information is available at Deception Island other
95 geophysical, geological, and geochemical information must be considered with
96 care in the final interpretation.

97 The aim of this study is to obtain reliable 3D frequency-dependent P -wave
98 attenuation images of the upper 4 km beneath Deception Island (South Shet-
99 land archipelago, Antarctica) by using a subset of the waveforms employed by
100 Ben-Zvi et al (2009) and Zandomeneghi et al (2009) to obtain velocity tomog-
101 raphy results. We will provide **new evidences that can be used in the future**
102 **in a new** geophysical interpretation ~~in terms of V_p and Q_p~~ by the compari-
103 son of the velocity and attenuation results with the current **and new** scientific
104 ~~literature~~ **results** focused on the formation and structure of the Island. ~~we~~

may discriminate the effects caused by sediments, fluids, cracks, and partially melted materials on the velocity and attenuation images in order to shed light on the structures feeding this volcanic area.

2 Deception Island: controversial interpretations

2 Deception Island: volcanological and geophysical models

Deception Island is an active volcanic island composed by rocks that date to less than 0.75 Ma and which suffered several historical eruptions in the last two centuries (Smellie 2001) (Fig. 1). Nowadays its low volcanic activity mainly consists of hot hydrothermal waters, fumarolic fields, and intense seismic activity composed by volcanic tremor, persistent long-period and volcano-tectonic seismicity (Vila et al 1992; Ortiz et al 1997; Ibáñez et al 2000; Carmona et al 2012).

The amount of information concerning the structures deeper than 1 km at Deception Island was recently increased with the TOMODEC active seismic experiment (e.g., Zandomeneghi et al 2009). Ben Zvi et al 2009 and Zandomeneghi et al 2009 use this vast dataset to obtain 2D and 3D images of P wave velocity structure in the entire area between depths of 0 to 10 km. Their results show strong deep (down to 8 km) lateral velocity variations, which are attributed to the presence of crustal magmatic systems with either partial melt regions and frozen intrusive bodies or sediment thickness variations and geothermal systems.

A large high velocity anomaly intersects the northwestern part of Deception Island (Telefon Bay, Fig. 1) and is associated with the crystalline basement of the South Shetland Islands platform (Zandomeneghi et al 2009; Pedrera et al 2012). The main feature of the velocity models, however, is an extended low P wave velocity anomaly, which intersects both the Port Foster bay and the eastern part of the island (Fig. 1). The anomaly, which lies under the sediment-filled basin in the center of the island, submerged by the Ocean, is interpreted as the image of an extensive shallow magma filled region (Ben Zvi et al 2009; Zandomeneghi et al 2009). Lopes et al (2014) suggest that Deception Island was actually formed above a magma chamber stretched under the influence of the regional transtensional regime with left lateral simple shear. The caldera collapse may have occurred in at least two phases. A small volume event occurred along the compressed flanks of the volcano edifice, followed by a large collapse event, which affected the stretched flanks of the volcano edifice.

The influence of a shallow magma chamber may still be detected with seismic observations, as the ones in apparent slowness and azimuth obtained by García Yeguas et al (2010) by using seismic arrays and active data. These authors admit that several details of their analysis remain unexplained for a correct interpretation. The continuous monitoring of the long period and volcano tectonic seismicity between 1990 and 2011 by means of array analyses shows in fact that the inferred velocity discontinuity in the center of the Is-

land may be associated with the ring fracture system bordering the collapsed caldera structure, that extends over the inner part of the island (Ibáñez et al 2000; Saccorotti et al 2001; Carmona et al 2012).

Regarding seismic attenuation, Vila et al (1995) obtained local attenuation parameters from both coda analysis and source parameters information. The authors show abnormally low coda Q values characterized by high frequency dependence in the inner bay of the island. They do interpret it as due to a hot magmatic intrusion produced during the most recent eruption, but the width of this intrusion is estimated to be only about 0.2 km. More recently Martínez-Arevalo et al (2003) estimated the seismic attenuation of both P and S waves at Deception Island, observing a predominance of scattering over intrinsic attenuation. They do interpret these results as produced by a zone of strong heterogeneity, as done in most volcanic areas (Dep Pezzo et al 2008), where the presence of magma patches cannot be excluded.

Prudencio et al (2013) obtained the regional 2D distribution of intrinsic and scattering attenuation of the Island by using the same waveform dataset employed to image its velocity structure and the diffusion model. The authors confirm the presence of a high scattering attenuation body below the inner bay of Deception Island, strongly interacting with the coda wave field, and which may be associated with magma.

Munoz Martin et al (2005) and Pedrera et al (2012) carried out magnetotelluric and gravimetric surveys on the island. The 3D resistivity models of Pedrera et al (2012) reveal an elongate conductor between 2 and 10 km east of Whalers Bay (Fig. 1), which they interpret as induced by a combination of partial melt and hot fluids. The inferred deep magma sill is connected to the surface by a large resistive path ending under Port Foster, spatially correlated with the velocity anomaly, and interpreted as a shallow magma chamber.

The above observations all support or, at least, consider the hypothesis of a shallow magma chamber beneath the center of the bay. However, new field data as well as a review of older seismically related measurements (e.g., seismic profiles, local and regional seismicity, etc.) confutes this hypothesis Marti et al (2013). The authors show that a polygonal structural network consisting of several pre-existing major normal faults controlled pre and post caldera volcanism on the island: hence, recent eruptions have been fed by small batches of deeper source magma. In this interpretation, eruptive intrusions provide the main heat source that sustains the current geothermal system inside its depression, which may be responsible for most of the present day observations.

The studies supporting the existence of a shallow magma chamber under Deception also recognize the relevance of hydrothermal activity on their geophysical and geological results. For example, Luzón et al (2011) obtain images of the shallow surface wave velocity structure of Deception Island by using correlations of ambient seismic noise. The results show that the volcano is composed of soft layers of pyroclastic deposits and sediments extending to a depth of about 400 m, while the deeper structure is highly variable in terms of velocities and layer depths; largest S wave velocities can be associated with

pre caldera structures and lowest S wave velocities may be related to the hydrothermal activity near the surface.

Kusakabe et al (2009) analyze stable isotope and noble gas data from fumarolic and bubbling gases and hot spring waters sampled from Deception Island. The results clearly show that magma at Deception Island was generated in the mantle wedge of a MORB type source. The fumaroles produce noble gas ratios higher than those of typical mantle derived gases, suggesting a strong influence of sediments in the subducting slab. The temperatures in the hydrothermal system below Deception Island range from 150 °C to 300 °C: these measurements show no contribution of magmatic water to the samples, hot spring waters being a mixture of local meteoric water and seawater.

As indicated above, many of the present efforts of several researchers are focused in the interpretation of the geophysical, geodetic and geochemical observations in terms of structural and volcanological framework of the volcano to understand its past and to infer a possible evolution and volcanic dynamic. These researchers integrated seismic observations, mainly low and high seismic velocities and contrast in attenuation, conductivity, gases and geodetical information. On the base of these observations there are mainly at the present two possible models that are coincident in the interpretation of the shallower structure (0-2 km) and they are in desagree in the interpretation of the deeper structure. In one of them the effects of fractured rocks and the existence of a geothermal system that hydrothermally altered the medium is detected up to 6 km depth (Martí et al 2013). In the other, the observed anomalies are interpreted as the effects of the presence of certain amount of melted rock/material with variable volume (e.g. Ben-Zvi et al 2009; Pedrera et al 2012; Muñoz Martín et al 2005).

2.1 Deep Geothermal effect

Recently, Martí et al (2013) on the base of new stratigraphy and petrological studies, with the revision of previous results proposed a model of the formation and internal structure of the Island. In reference to the present internal structure, the authors show that a polygonal structural network consisting of several pre-existing major normal faults controlled pre- and post- caldera volcanism on the island. They defend that the formation of the caldera caused the destruction of the associated magma chamber and hence, recent eruptions have been fed by small batches of deeper-source magma. In their interpretation, a large hydrothermal system developed in the interior of the depression using highly fractured pre-caldera basement and syn-caldera rocks. The authors suggested that the current hydrothermal system inside its depression, which may be responsible for most of the present-day observations up to 6 km depth.

2.2 Existence of melted material

236 Mostly of the geophysical and geodetic studies performed in the area ob-
237 served the existence of high contrast of the physical properties studied and
238 these anomalies have an evident presence in the central part of the island
239 (bellow Port Foster). These anomalies extend up to 6-10 km depth and their
240 interpretations include the existence of partial melted rocks at depths 2-10
241 km.

242 **Seismic velocity observations:** Ben-Zvi et al (2009) and Zandomeneghi
243 et al (2009) used the data-set provided by the TOMODEC active seismic
244 experiment to obtain 2D and 3D images of P-wave velocity structure in the
245 entire area of Deception Island between depth of 0 to 10 km. Their results show
246 strong deep (down to 8 km) lateral velocity variations, which are attributed
247 to the presence of crustal magmatic systems with either partial melt regions
248 and frozen intrusive bodies or sediment thickness variations and geothermal
249 systems. The authors indentified a large high-velocity anomaly intersects the
250 northwestern part of Deception Island (Telefon Bay, Fig. 1) that was associated
251 with the crystalline basement of the South Shetland Island platform. However,
252 the main feature of the velocity models is an extended low P-wave velocity
253 anomaly, which intersects both Port Foster bay and eastern part of the island
254 (Fig. 1). The same authors interpret the shallow low velocity anomalies (0-2
255 km) as the effect of sediment-filled basin, hydrothermal activities, fractured
256 materials from the caldera collapse and others. Ben-Zvi et al (2009) (pp.78) on
257 the base of numerical simulations observed that the velocity anomalies bellow
258 2 km depths are compatible with the presence of partial melted materials (up
259 to 15 melted) and with a maximum volume of up 20 km³. Zandomeneghi et
260 al (2009) agree this interpretation.

261 **Seismic attenuation observations:** Regarding seismic attenuation, Vila
262 et al (1995) obtained local attenuation parameters from both coda analysis and
263 source parameters information. The authors show abnormally low coda-Q val-
264 ues characterized by high frequency dependence in the inner bay of the island.
265 They do interpret it as due to a hot magmatic intrusion produced during the
266 most recent eruption, but the width of this intrusion is estimated to be only
267 about 0.2 km³. More recently Martinez- Arevalo et al (2003) estimated the
268 seismic attenuation of both P- and S-waves at Deception Island, observing
269 a predominance of scattering- over intrinsic- attenuation. They do interpret
270 these results as produced by a zone of strong heterogeneity, as done in most
271 volcanic areas (Del Pezzo 2006), where the presence of magma patches can-
272 not be excluded. Recently, Prudencio et al (2013) obtained the regional 2D
273 distribution of intrinsic and scattering attenuation of the Island by using the
274 same waveform dataset employed to image its velocity structure and the diffu-
275 sion model. The authors confirm the presence of a high scattering attenuation
276 body below the inner bay of Deception Island, strongly interacting with the
277 coda wave-field, and which may be associated with magma compatible with
278 the existence of magma.

279 **Gravimetric and magnetotelluric observations:** Muñoz-Martin et al
280 (2005) show a very low density anomaly in both magnetic and gravity anomaly
281 maps of Deception Island. The authors interpreted this anomaly as a partially

melted intrusive body and they estimated the top of this body at 1.7 km depth using Euler deconvolution techniques. The 3D resistivity models of Pedrera et al (2012) reveal an elongate conductor between 2 and 10 km east of Whalers Bay (Fig. 1), which they interpret as induced by a combination of partial melt and hot fluids. The inferred deep magma sill is connected to the surface by a large resistive path ending Port Foster, interpreted as a shallow magma chamber.

3 Data, method, and inversion setting

3.1 Data and ray tracing.

The waveforms used in this study are a subset of the ones used by Zandomenighi et al (2009) to obtain 3D velocity images by using a shortest-time ray tracing and a LSQR algorithm inversion. The authors choose two different model parametrizations. The first grid has coarser parametrization (250 m), it is centered on Deception Island and extends 53 km from West to East (WE), 52 km from South to North (SN), and down to 12 km depth. A smaller grid of 100 m step includes Port Foster and the nearest surroundings, and extends 12 km WE, 14 km SN, and down to 7 km depth. In order to compare the velocity and attenuation models we use a grid having the same lateral extension of the first grid in Zandomenighi et al (2009).

Amplitude data are strongly frequency dependent. We show four recordings produced by a shot in the center of the bay (blue star) and registered at stations M, F, J, and H (Fig. 2). The stations record waveforms with excellent signal-to-noise ratios (larger than 10) for the entire signal ~~after~~ above 8 Hz only. However, both Vila et al (1995) and Prudencio et al (2013) show abnormally-low attenuation values at high frequencies in the Port Foster bay, where we focus our attention. Due to this strong attenuation we cannot provide reliable attenuation models of structures as deep as 4 km at frequencies larger than 10 Hz.

We obtain the attenuation model after filtering data in the 4-8 frequency band (6 Hz ~~central frequency~~). Considering the lowest measured velocities in the inner bay, ~~the signal wavelength associated with~~ this frequency band safely allows to depict structures of the order of 1 km dimension at 4 km depth. As shown by Prudencio et al (2013) this frequency band also provides stable results for the ~~attenuation separate~~ measurements of both intrinsic and scattering attenuation ~~from coda wave data~~. ~~even if the data are affected by large uncertainties~~

We use the same Thurber-modified ray-bending approach described, e.g., by De Siena et al (2010) in the 3D sparse velocity model of Zandomenighi et al (2009) (Fig. 3). ~~The ray crossing at 5 km depths is still adequate for a tomographic approach (Fig. 3) but the increased linearity of the rays sums to the strong dispersion of coherent information with increasing depth.~~ ~~space density of the rays at depth of 5 km is still sufficient for correctly performing the tomography inversion (Figure 3).~~ On the other hand, observational data associated with these paths show highly incoherent estimates even for paths

326 **crossing almost the same volumes.** Therefore, our analysis and final interpretation
 327 is restricted to depths of 1 to 4 km: these analysis may provide hint on
 328 deeper structures once compared with other measurements.

329 3.2 *P*-wave attenuation tomography with the coda normalization method

330 The coda-normalization (CN) method has been first applied to the single-
 331 station estimate of the total *S*-wave inverse quality factor Q along the seismic
 332 path by Del Pezzo et al (2006) in the Mount Vesuvius volcanic area. The
 333 single-path attenuation is obtained in a given frequency range with central
 334 frequency f_c by measuring the direct-*S* energy (E_k^s) and the coda-*S* energy
 335 ~~from~~ **in a time window centered around** a given lapse time t_c ($E_k^c(f_c, t_c)$), and
 336 calculating their ratio. The single-path CN equation is:

$$\frac{1}{\pi f_c} \ln\left(\frac{E_k^s(f_c)}{E_k^c(f_c, t_c)}\right) = K(f_c, t_c, \theta, \phi) - \frac{2}{\pi f_c} \gamma \ln(r_k) - 2 \int_{r_k} \frac{dl}{v(l)Q(l)} \quad (1)$$

337 where r_k is the total length of the k^{th} ray, γ is the geometrical spreading, and
 338 $v(l)$ is the velocity of the medium measured along the ray-path. $K(f_c, t_c, \theta, \phi)$
 339 takes into account the effect of the source radiation pattern, described by the
 340 take-off angle (θ) and azimuth (ϕ) and is the only other unknown variable
 341 (apart for Q) in the equation. As in given frequency bands diffraction effects,
 342 waveguides, and surface waves could affect the exponent γ of the geometrical
 343 spreading we choose to invert this parameter with the inverse average quality
 344 factor (La Rocca et al 2001; Morozov 2011; De Siena et al 2014).

345 As shown by Yoshimoto et al (1993) we can extend the CN method to the
 346 measurement of *P*-wave average attenuation (the *P*-wave quality factor, Q_p).
 347 We use active sources, that is, only *P*-waves are produced. We can reasonably
 348 assume a spherical source radiation pattern, hence, $K(f_c, t_c, \theta, \phi) = K(f_c, t_c)$,
 349 leaving Q_p as the only unknown in the inversion problem. We can thus apply
 350 the CN method to *P*-wave attenuation tomography under three assumptions:

- 351 – the small *P*- and *S*-wave mean free paths in the volcanic structures allow
 352 for a quick conversion of *P*-wave energy into coda energy,
- 353 – the seismic paths traveled by the waves producing the energy ratios filtered
 354 in the chosen frequency band can be approximated by a ray (curve),
- 355 – the lapse-time from origin is large enough to measure coda energy out of
 356 the *P*-wave transient regime.

357 The energy ratios vs. travel times behaviour reveal no evident anomalous
 358 energy-ratio increase localized in space at 6 Hz, indicative of anomalous co-
 359 herent effects in the coda envelopes (De Siena et al 2014). As the lapse time
 360 t_c strongly influences the estimates of the average parameter if it is set to
 361 short lapse-times (Calvet and Margerin 2013) we set the start of the coda
 362 time-window of length 3 s to a lapse-time of 12 s. The *P*-energy time window
 363 is set to 1.5 s. The waveforms were selected depending on the coda-to-noise
 364 ratio (always larger than 1.5) at 6 Hz.

365 The final data-set is comprised of 20293 vertical seismic waveforms. The in-
 366 version of the energy ratios for the average parameters provides an average Q_p
 367 of 29; in the following we will discuss the variations with respect to the inverse
 368 of the average quality factor in the 3D space (ΔQ_p^{-1}), a direct measurement of
 369 attenuation. By considering these observations as well as the ideal distribution
 370 of our sources we invert the energy ratios for the attenuation parameters with
 371 the MuRAT code in a single-step inversion (De Siena et al 2014).

372 4 Synthetic tests

373 We want to discriminate the resolution we effectively achieve on a high at-
 374 tenuation anomaly in the center of the bay down to 4 km depth (Fig. 4). We
 375 start testing the resolution of the ΔQ_p^{-1} results assuming as input synthetic
 376 anomaly a high attenuation region in the centre of the island, roughly designed
 377 on the results of the velocity tomography (Figure 4, high attenuation corre-
 378 lated with high velocity). Hence, we impose a $8 \times 8 \times 4 \text{ km}^3$ volume of low quality
 379 factor under Port Foster. We generate synthetic P -to-coda energy ratios and
 380 we add Gaussian random error with zero mean and 3 times the standard de-
 381 viation, equal to the 20% of the data value. We invert the synthetic data only
 382 in blocks crossed by at least 5 rays. We show the results on four horizontal
 383 slides at different depths (Fig. 4).

384 In order to test the resolution in the entire region we also perform a checker-
 385 board test, whose output is shown on the same 4 horizontal slices used in Fig. 4
 386 (Fig. 5, third column). We add the same amount of Gaussian random error to
 387 the synthetic P -to-coda energy ratios calculated from a checkerboard synthetic
 388 structure with 2 km node spacing, starting at 0 km, and having quality factors
 389 equals either to 100 or 1000. The checkerboard and synthetic anomaly test in-
 390 puts and outputs are also shown on SN and WE vertical sections, crossing the
 391 inner bay (Fig. 3, dotted gray line).

392 The checkerboard test results are well resolved everywhere between depths
 393 of 1 and 3 km, while smearing affects the output at 4 km depth, especially
 394 in the regions contouring the island (Fig.s 5). The synthetic anomaly test is
 395 well resolved down to 4 km depth except for some smoothing on the southern
 396 and western sides of the images, between depths of 1 to 3 km (Fig.s 4 and 6).
 397 We conclude that we have good resolution in the volume under study. Also, a
 398 high attenuation anomaly, located in the center of the bay and as deep as 4
 399 km, can be obtained by the inversion of real data.

400 5 Results and joint interpretation with the geological and 401 geophysical results.

402 Fig. 5 shows 4 horizontal slices through the velocity and attenuation models
 403 down to a depth of 4 km (left-hand and central columns). Fig. 6b,c shows
 404 two vertical sections of these models, following the WE and SN directions as

shown in Fig. 3 (gray dotted line). The P -wave percent velocity variations ($\% \Delta V_p$) are calculated by the P -wave velocity model of Zandomenighi et al (2009). The interpretation of our results is based on the analysis of the largest attenuation anomalies in the regions of major volcanological interest (Fig. 7).

In order to correlate the velocity and attenuation anomalies with those obtained by other geophysical and geological studies we discuss the results under the Oceanic Crust and ~~calderic rim~~ **caldera structure** separately from the ones under the Port Foster. We also separate the discussion of the anomalies under Port Foster bay in two different depth ranges (between depths of 1 and 2 km and between depths of 3 and 4 km).

5.1 Oceanic Crust and ~~caldera rim~~ **caldera structure**

No unique high-attenuation anomaly larger than 2 km is visible under the Oceanic Crust contouring the island. An arc-shaped volume of small (2 km average dimension) high-attenuation anomalies is located northeast of Deception at a depth of 1 km (Fig. 5). This volume, located in a low-velocity zone, is partially visible in the 2 km tomograms. (Zandomenighi et al 2009) interpret the vast superficial low-velocity anomaly northeast of the island (1 to 2 km depth, Fig. 5, left-hand column) as a zone of accumulation for sedimentary materials **and hydrothermal activity**. From the depth extension and location of the high-attenuation arc-shaped volume we confirm this interpretation, in the sense that the high attenuation anomaly may actually locate the inner boundary of the sedimentary structures **and hydrothermal interactions**.

Most of the source energy recorded near this boundary crosses the Port Foster bay, that is, the most attenuating structure in the entire region (Vila et al 1995; Martinez-Arevalo et al 2003). The fractured caldera as well as the faults contouring the inner bay may also reflect or diffract direct energy. Hence, we may not expect to image the exact lateral extension of these sediments: we may safely assume that velocity tomography provides more reliable information on these structures.

Under the south-south-eastern part of the caldera ~~rim~~ **structure**, which constitutes the part of Deception emerged out of the Ocean, we observe the largest attenuation contrast, marking the entire depth range (e.g., Figs 6c and 7 SN). The low attenuation visible under the caldera ~~rim~~ defines an almost vertical boundary with the high attenuation medium under Port Foster, in strong correlation with the location of deep normal faults. The southern part of Deception is also affected by large smearing (Fig. 6d), induced by the large velocity contrast affecting the deep geometry of each source-station ray passing through it.

Pedrerá et al (2012) obtain a vast conductive body extending SE of the Island between depths of 2 and 12 km. The authors suggest emplacement of melt in this volume driven by an ENE–WSW oriented and SSE dipping regional normal fault. An almost vertical low-velocity and high-resistivity anomaly between depths of 2 and 6 km is located below Port Foster, connecting the vast

southeastern high-resistivity anomaly with the center of the island. The vertical attenuation contrast is laterally disposed above the northwestern limit of the deep high resistivity anomaly (Fig. 7).

~~We infer that the south-south-eastern part of the Island may actually be a fluid/melt feeding path for the caldera (Ben-Zvi et al 2009; Zandomeneghi et al 2009; Pedrera et al 2012). Our results are compatible with previous studies (Ben-Zvi et al 2009; Zandomeneghi et al 2009; Pedrera et al 2012) affirming that the south-south-eastern part of the Island may contain a certain volume of a fluid/melt which may be the feeding path for the caldera.~~ The section of this path, which should be connected to the center of the island and present high attenuation, reduces to our node spacing in the attenuation images at 4 km depth (Fig. 5, 4km). ~~As suggested by Martí et al (2013) Additionally, our results are also compatible with other interpretation provided by Martí et al. (2013) in which~~ the deep feeding structures may simply heat the upper crustal systems, where meteoric waters both penetrate and circulate producing the high-attenuation anomaly in the centre of the caldera (Fig. 7).

Deception faces the Bransfield Through from northwest (Martí et al 2013). The collapsed part of its caldera ~~rim structure~~ corresponds to the northwestern margin of the Through as well as to both steep almost-vertical normal faults and strong attenuation contrasts (Fig. 7, upper-right panel). Velocity and resistivity tomograms show clear low-velocity and high-resistivity connections of the upper anomalies with deeper vast high-resistivity regions, extending south-east of the island (Fig. 7, vertical section). ~~We infer that the feeding system, through which fluids and melt materials either pass or heat the upper crustal materials, starts south-east of the Island at around 6 km Pedrera et al (2012). Our results are in concordance with those obtained by Pedrera et al (2012) which suggested that the feeding system, through which fluids and melt materials either pass or heat the upper crustal materials, starts south-east of the Island at around 6 km.~~ The main connection with the surface rises almost vertically towards the southeastern margin of the Island (Zandomeneghi et al 2009; Pedrera et al 2012), passing through the high-attenuation contrasts southeast of the Island (Fig. 7). We discuss in the next two sections if, how, and where the deep melt materials (magma) are stored in the first 4 km under Deception.

5.2 From depths of 1 to 2 km under Port Foster

The Port Foster Bay (inner bay of Deception Island, Fig. 1) is dominated by a large ΔQ_p^{-1} positive anomaly, that is, by high attenuation, down to a depth of 2 km (Fig. 5, central column, red). In this depth range the high-attenuation volume is contoured by average-to-low attenuation structures, mainly corresponding to the exposed caldera rim (Figs. 5 and 6c). Zandomeneghi et al (2009) and Luzón et al (2011) both propose that unconsolidated volcanoclastic and volcano-sedimentary materials, possibly producing high attenuation, extend down to 1.2 - 1.4 km depth. We remark, ~~however,~~ that the anomaly in

491 the centre of the bay shows much higher attenuation than the surroundings.
492 This is particularly relevant if we compare the results in the central bay with
493 the arc of high attenuation located northeast of the island, where low velocities
494 are also interpreted as induced by sediments (Zandomeneghi et al 2009).

495 The strong P -wave attenuation is paired with a strong scattering signa-
496 ture (obtained by Prudencio et al (2013) under the bay) and suggests that
497 materials with higher attenuation capacity than sediments, like ~~either fluids~~
498 **hydrothermal interations or magma**, intrude the first 2 km depth under the
499 Port Foster bay. The top of a resistivity anomaly obtained by Pedrera et al
500 (2012) resembles pretty well the low velocity and high attenuation structure
501 under the bay at a depth of 2 km (Fig. 5, see also Zandomeneghi et al (2009)).
502 ~~Both Zandomeneghi et al (2009) and Pedrera et al (2012) infer that their~~
503 ~~anomalies are mainly induced by a shallow magma fluid chamber.~~

504 Getting S-wave velocity information is ~~critical~~ **important** for the interpreta-
505 tion of the attenuation anomalies. ~~The only measurements which may provide~~
506 ~~us information on the transverse velocity wave field between depths of 1 and~~
507 ~~2 km are the surface wave velocities obtained by using noise measurements at~~
508 ~~different inland sites near the inner bay Luzon et al(2011).~~ **Luzon et al (2011)**
509 **provide us information on the transverse velocity wave-field between depths**
510 **of 1 and 2 km.** The lowest S-wave velocities (related in the interpretation
511 of Luzón et al (2011) to the alterations produced by hydrothermal activity)
512 are near Chilean station (Fig. 1) northeast of the bay. On the contrary, the
513 largest velocities occur near the SW caldera border, revealing the presence of
514 compact materials at shallow depths. The low velocity anomaly obtained by
515 Luzón et al (2011) at 1 km matches with the high-attenuation unique anomaly
516 shifted towards the north part of the bay.

517 De Siena et al (2010) depict zones of fluid accumulation coupled to a sur-
518 rounding network of normal faults beneath Pozzuoli (Campi Flegrei, Italy),
519 where the correlation of high attenuation and high V_p/V_s anomalies (Vanorio
520 et al 2005) is striking. This high attenuation anomaly is contoured by a hard
521 rock volume and associated with the caldera rim structure: this image is very
522 similar to the one we observe at Deception (compare our results with De Siena
523 et al (2010), Fig. 7c, markers X4, X5, and X6). In De Siena et al (2010) the
524 presence of melt is restricted to a small volume located at a depth of about
525 4 km embedded in a hard rock volume, and heating the geothermal system
526 under Pozzuoli.

527 The lateral extension of the high attenuation anomaly at Deception is ac-
528 tually coincident with the bathymetry of the floor of the bay (Fig. 6a), which
529 reveals a broad uplift of the eastern side of the caldera (Cooper et al 1999). As
530 proposed by Barclay et al (2009) ~~and remarked by Martí et al (2013)~~ bathy-
531 metric results could be caused by sediment supply rates **and hydrothermal**
532 **alterations** from the east of the island or by a trap-door caldera deformation
533 with its minimum subsidence in the east. Both these causes are compatible
534 with permeation of local meteoric water and seawater in the intra-caldera
535 formation.

536 ~~Important indications on the absence of a large magmatic chamber between~~
537 ~~depths of 1 to 2 km come from~~ Other additional evidences of the nature of
538 sediment deposits, volcanoclastic materials and hidrothermal alteration effects
539 on the first 2 km shallow part of the caldera floor, is obtained by the study of
540 some geochemical aspects of the area as the study of isotopes and noble gas
541 data from fumarolic and bubbling gases and hot spring waters (Kusakabe et
542 al 2009). *He* and *CO*₂ are mainly of mantle origin, with no contribution of
543 magmatic water to water and gas samples, hot spring fluids being a mixture
544 of local meteoric water and seawater. Kusakabe et al (2009) infer that these
545 results are due to the existence of a heated hydrothermal system, with different
546 temperatures in the depth range between 1 and 2 km.

547 The shape of the high attenuation anomaly, contoured by the low-attenuation
548 caldera rim between depths of 1 and 2 km (Fig.s 5 and 6) is similar to the
549 one retrieved under different calderas and associated with the presence of
550 hydrothermal fluids alteration. The large low-velocity and high-attenuation
551 structure in the bay (Fig.s 5 and 6b,c) correlates well with high resistivity,
552 high scattering attenuation, and low S-wave velocities. ~~If we also consider the~~
553 ~~absence of magmatic water from water and gas samples we may infer that~~
554 ~~the~~ Therefore, attenuation anomaly shows a portion of the collapsed caldera
555 center permeated by a geothermal reservoirs, at least between depths of 1 and
556 2 km.

557 5.3 From depths of 3 to 4 km under Port Foster

558 Low velocity and high attenuation anomalies are ~~only weakly correlated~~ less
559 strong at depths larger than 2 km under Port Foster (Fig.s 5 and 6). The
560 percent velocity variations show a continuous vertical anomaly between depths
561 of 3 and 4 km, while the high-attenuation anomaly is shaped as a spherical-
562 like system having its basis approximately at 3 km depth (Fig. 6b,c). No large
563 unique high-attenuation anomaly is visible at a depth of 4 km in the centre of
564 the bay (Fig.s 5 and 6c). High-attenuation anomalies with lateral extensions
565 of the order of our node spacing connect the upper high attenuation semi-
566 spherical anomaly with depth. Our assumption is that seismic attenuation is
567 more sensitive to the presence of deep melt and fluids than seismic velocity,
568 while velocity tomography is able to sample larger depths (Hansen et al 2004;
569 De Siena et al 2010; Muksin et al 2013).

570 In their 2D and 3D resistivity maps Pedrera et al (2012) also reveal an
571 ENE–WSW elongated conductor located between 2 and 6 km depth beneath
572 the Port Foster bay, which they interpret as induced by a combination of
573 partial melt and hot fluids. The depth resolution of the magnetotelluric model,
574 which defines quite precisely the top of melt/fluid regions, is affected by the
575 resistivity of the superficial highly-resistive marine layers. This may cause an
576 incorrect depth definition of the highly resistive structures. As in attenuation
577 tomography we use ray-dependent measurements we assume we provide higher

578 resolution than in magnetotelluric imaging, again at the expense of depth
579 sampling.

580 The attenuation tomograms clearly show that the anomaly extends down
581 to a maximum depth of 3 km as a unique hemispherical body. The depth
582 extension and shape of the high attenuation anomaly at depths of 3 to 4 km is
583 similar to the ones observed in other areas, e.g., by De Siena et al (2010) in the
584 Campi Flegrei caldera, by Muksin et al (2013) in the Tarutung Basin, and by
585 Bohm et al (2013) in the Kendeng Basin. These observations are always related
586 to sedimentary or volcanoclastic deposits overlying active geothermal and gas
587 reservoirs. However, other studies, interpret this high attenuation anomaly
588 and low velocity body as the presence of shallow partial melted magma body
589 such as Koulakov et al (2009) and Jaxybulatov et al (2014) in Toba caldera
590 or Ohlendorf et al (2014) in Okmok Volcano. In Okmok volcano the authors
591 found the same pattern of velocity and attenuation observed in Deception
592 Island and they interpreted the shallow part of the anomaly (surface to 2 km)
593 as caldera fill, groundwater and small pods of magma and the deeper part of
594 the anomaly (from 4 to 6 km) as a magma storage zone. This geodynamic
595 model is compatible with the subduction processes or slab rollback suggested
596 by Maestro et al (2007).

597 ~~We infer that the low velocity and high resistivity conductor imaged by~~
598 ~~Zandomeneghi et al (2009) and Pedrera et al (2012) between 3 and 6 km ac-~~
599 ~~tually shows a feeding path of hot lower crustal or mantle materials (Fig. 7).~~
600 ~~However, the shape of the high attenuation anomaly as well as its maximum~~
601 ~~extension to 3 km as a unique hemispherical body bordering the rim better fits~~
602 ~~an interpretation in terms of an active geothermal system filling the cracked~~
603 ~~collapsed caldera center (Fig. 7). As indicated previously in section 2 and~~
604 ~~above, our results are compatible with both proposed models. The modelled~~
605 ~~volume of melted rocks of Ben-Zvi et al (2009) (less than 15-20 km³) in depth~~
606 ~~can coexist with other effects as a network of magma and fluid filled batches~~
607 ~~of size either lower than or equal to our resolution seems the more reliable~~
608 ~~explanation for the absence of a unique high attenuation anomaly down to 4~~
609 ~~km. This network could be visible as a unique velocity and conductive anomaly,~~
610 ~~which may provide the main heat source that sustains the geothermal system~~
611 ~~in the first 3 km of the crust (Martí et al 2013).~~

612 6 Conclusions

613 ~~We obtain and interpret the 3D P -wave attenuation model of Deception Is-~~
614 ~~land by using different geophysical, geological, and geochemical observations,~~
615 ~~in order to discriminate the nature and extension of volcanological structures,~~
616 ~~especially melt and fluid accumulation regions. Sediments filling the upper two~~
617 ~~km northeast of the island produce a small boundary approximately following~~
618 ~~the caldera rim.~~

619 ~~We infer that the strong attenuation contrast under the southeastern part~~
620 ~~of the island shows the location and effects of normal faults, which drive~~

~~melt/fluid materials in the upper two km of the crust, and meteoric waters circulation in the lower crust. A large resistivity anomaly having its top between 5 and 6 km depth has its northwestern margin directly below this contrast. In this interpretation, between depths of 4 and 6 km, highly resistive and low velocity anomalies still show the feeding path of the caldera. However, the attenuation images exclude the presence of a large magma accumulation region at 4 km.~~

~~The most relevant anomaly in the attenuation model is the unique high-attenuation spherical like structure beneath the Port Foster bay, its lateral extension well correlated with the Port Foster bathymetry. Our results discriminate both the lateral and depth extension of either a magma or a fluid-filled zone centered beneath the northeastern part of the submerged island center. The anomaly has a maximum depth extension of 3 km and is generally associated with low P and S wave velocities, high resistivity, and high scattering attenuation. Hot spring waters collected near the anomaly are a mixture of local meteoric water and seawater, showing no magmatic contribution. The 3D shape of the anomaly, contoured by the rim, is similar to the one observed in other calderas and geothermal systems.~~

~~The problem of assessing the presence (or absence) of magma in high attenuation anomalies is equivalent to the problem of defining which percentage of magma should be contained in a structure to define it as a magma chamber. With our method we are not able to discriminate exactly these percentages. Nevertheless, the results of our analysis let us lean towards an interpretation in terms of a cracked medium filled with sediments and geothermal fluids inside the caldera depression with smaller percentages of magma, down to 3 km depth.~~

~~In our interpretation, the system is mainly heated by smaller, deeper magma related anomalies, located inside the low velocity and high resistivity path below 3 km. This path is produced by the vast deep high resistivity region southeast of the island, and may provide the main path for deeper rising magma derived heat. In order to either confirm or confute this interpretation the addition of new geological, geophysical, and geochemical data (in particular spatial models of P to S velocity ratio variations) is critical.~~

In the present work we obtain the 3D P-wave attenuation model of Deception Island by using coda normalization method. The methodology used in this study is stable, robust and reliable. The reliability of the method is based on the similarity of results with other studies. The study of S-waves and V_p/V_s distribution might better constrain the inner structure of the island.

We have provided new results showing the complex attenuative structure of the island with the presence of bodies of low and high attenuation. As in the velocity tomography, we find a limitation in the range of depth that we are able to solve due to the structure of the thinned oceanic crust region where the Moho is 4-5 km depth and it implies a physical barrier.

One of the most important remarks is the presence of high attenuation body in the center of the island which extends from the surface to our resolution limit. The interpretation of this anomaly in the first two kilometers agrees

almost all researchers who have worked on the island and is associated with the effects of sedimentary and volcanoclastic deposits, hydrothermal interactions and highly fractured material.

The interpretation of the deeper structure is more complex, mainly due to the lack of S-waves data. Thus, our results are consistent with two possible models. In the first, the high attenuation and low velocity is due to a hydrothermal system effects. On the other, this anomaly is interpreted as the existence of a partially molten magmatic body. A combination of these two models is also compatible with our results. It will be necessary to continue working to incorporate data from S waves or other methodologies to give light to the interpretations.

7 Fig. captions

Fig. 1: Regional setting and location of Deception Island in the South Shetland Islands archipelago, Antarctica (upper two panels). Bottom panel: Toponyms (bold italics), historical eruption sites (white on black rectangle), and research stations active or destroyed by the recent eruptions (regular bold), are shown on the contour map of Deception Island.

Fig. 2: Configuration of the TOMODEC seismic tomography experiment. a) Land and ocean bottom seismometers (red triangles) and shots locations (gray lines) are drawn on a contour map of the island. In the top right panel we a zoom on the center of the island (Port Foster bay). b): 3D and 2D source station ray paths obtained by using a Thurber modified ray bending approach. All the events are approximately located at 0 km depth and produced by air-guns. The red contour map imposed on the rays shows the location and shape of Deception Island with respect to the experiment setting.

Fig. 3: The vertical records of a seismic shot produced on the 8 of January 2005, located in the center of the Port Foster Bay (blue star), and recorded at four seismic land stations (M, F, J, H). The gray dotted line crossing near the center of the bay indicate the location and direction of the vertical sections shown in Fig. (6). The panels on the right show the signal spectrum (S, blue lines) and noise spectrum (N, red lines) for each recording.

Fig. 2: The vertical records of a seismic shot produced on the 8 of January 2005, located in the center of the Port Foster Bay (blue star), and recorded at four seismic land stations (M, F, J, H). The gray dotted line crossing near the center of the bay indicate the location and direction of the vertical sections shown in Fig. (6). The panels on the right show the signal spectrum (S, blue lines) and noise spectrum (N, red lines) for each recording.

Fig. 3: Configuration of the TOMODEC seismic tomography experiment. a) Land and ocean bottom seismometers (red triangles) and shots locations (gray lines) are drawn on a contour map of the island. In the top-right panel we a zoom on the center of the island (Port Foster bay). b): 3D and 2D source-station ray-paths obtained by using a Thurber-modified ray-bending approach. All the events are approximately located at 0 km depth and produced by air-

710 guns. The red contour map imposed on the rays shows the location and shape
 711 of Deception Island with respect to the experiment setting.

712 **Fig. 4:** Upper panel: The synthetic anomaly test input is designed to show
 713 the reproducibility of a simplified deep high-attenuation anomaly under the
 714 Port Foster bay. The high attenuation anomaly has a dimension of $8 \times 8 \times 4 \text{ km}^3$
 715 and is characterized by a quality factor of 3. Lower panels: four horizontal slices
 716 through the output of the synthetic anomaly test taken at different depths with
 717 respect to the sea level. The ΔQ_p^{-1} grey scale shows the variations with respect
 718 to the average quality factor.

719 **Fig. 5:** The results of velocity tomography (Zandomenighi et al 2009, left-
 720 hand column), of the attenuation tomography (central column) and the output
 721 of the checkerboard test (right-hand column) are shown on four horizontal
 722 slices taken at different depths. The left-hand color scale shows the percent
 723 variations of the velocity model with respect to its average. Both the central
 724 color scale and the right-hand grayscale show the variations of the attenuation
 725 model with respect to the average quality factor. The contour of Deception
 726 Island is over-imposed on each panel.

727 **Fig. 6:** Bathymetry (a), velocity model (Zandomenighi et al 2009, b), at-
 728 tenuation model (c), and the synthetic tests (d) are all shown on two vertical
 729 sections crossing the Island (gray dotted lines in Fig. 3). The vertical scale in
 730 the velocity and attenuation images is enlarged for clarity. b) The color scale
 731 shows the percent variations of the velocity model with respect to its average.
 732 c) The color scale shows the variations of the attenuation model with respect
 733 to the average quality factor. d) The ΔQ_p^{-1} grey scale shows the variations
 734 with respect to the average quality factor. The inputs are shown above the cor-
 735 responding outputs for both the checkerboard test and the synthetic anomaly
 736 test. The input of the synthetic anomaly test is described in the caption of
 737 Fig. 4.

738 **Fig. 7:** Schematic interpretation of the attenuation model, carried out
 739 with reference to the 3D velocity (Zandomenighi et al 2009) and resistivity
 740 (Pedrera et al 2012) models, and constrained by other geophysical, geological,
 741 and geochemical observations, as described in the text. In the upper-right panel
 742 we show a horizontal section of the region taken at 8 km depth and depicting
 743 the portion of the Bransfield Through as well as the horizontal contour of
 744 the high resistivity anomaly contained in the region under study. We also
 745 infer from our analysis both meteoric water circulation in the upper crust and
 746 heat rising towards surface. We depict the depth dependence of the anomalies
 747 described in the text on two vertical sections, taken between depths of 0 and
 748 10 km and crossing the Island (gray dotted lines in Fig. 3). Below a depth of
 749 4 km the sketch is based on the 3D velocity and resistivity results only. Below
 750 5.5 km the sketch is based on the resistivity model only.

751 **Acknowledgements** We gratefully acknowledge editor Dr Rycroft, Prof. Martí and one
 752 anonymous reviewer whose useful suggestions greatly improved the manuscript. This work
 753 has been partially supported by the Spanish project Ephestos, CGL2011-29499-C02-01; by
 754 the EU project EC-FP7 MEDiterranean SUpersite Volcanoes (MED-SUV); by the Basque

755 Government researcher training program BFI09.277 and by the Regional project ‘Grupo de
756 Investigacin en Geofísica y Sismología de la Junta de Andalucía, RNM104’. Edoardo del Pezzo
757 has been partly supported by DPC-INGV projects UNREST, SPEED and V2 (Precursori).
758 We also thank Christine Thomas, Ralf Hetzel, and Stephan Klemme for the important
759 suggestions regarding both the method and the interpretation.

760 References

- 761 Aki K, Richards P (1980) Quantitative Seismology - Theory and Methods. W. H. Freeman,
762 San Francisco
- 763 Almendros J, Ibez J, Alguacil G, Del Pezzo E, Ortiz R (1997) Array tracking of the volcanic
764 tremor source at deception island, antarctica. *Geophysical Research Letters* 24:3069–
765 3072
- 766 Barclay A, Wilcock WSD, Ibáñez J (2009) Bathymetric constraints on the tectonic and vol-
767 canic evolution of Deception Island Volcano, South Shetland Islands. *Antarctic Science*
768 21:153–167
- 769 Ben-Zvi T, Wilcock WSD, Barclay A, Zandomenighi D, Ibáñez J, Almendros J (2009) The
770 P wave velocity structure of Deception Island, Antarctica, from two dimensional seismic
771 tomography. *Journal of Volcanology and Geothermal Research* 180:67–80
- 772 Benitez MC, Ramirez J, Segura JC, Ibez J, Almendros J, Garca-Yeguas A, Corts G (2007)
773 Continuous hmm-bases seismic-event classification at deception island, antarctica. *Geo-*
774 *science and Remote Sensing, IEEE Transactions* 45:138–146
- 775 Berrocoso M, Prates G, Fernandez-Ros A, Garca A (2012) Normal vector analysis from
776 gnss-gps data applied to deception volcano surface deformation. *Geophysical Journal*
777 *International* 190:1562–1570
- 778 Bohm M, Haberland C, Asch G (2013) Imaging fluid-related subduction processes be-
779 neath Central Java (Indonesia) using seismic attenuation tomography. *Tectonophysics*
780 590:175–188
- 781 Calvet M, Margerin L (2013) Spatial variations of seismic attenuation in the Pyrenees:
782 coda Q and peak delay time analysis. *Bulletin of Seismological Society of America*
783 103:doi:10.1785/0120120,239
- 784 Carmona E, Almendros J, Pea JA, báez JM (2010) Characterization of fracture systems
785 using precise array locations of earthquake multiplets: An example at Deception Island
786 volcano, Antarctica. *Journal of Geophysical Research: Solid Earth* 115
- 787 Carmona E, Almendros J, Serrano I, Stich D, Ibáñez J (2012) Results of seismic monitoring
788 surveys of Deception Island volcano, from 1999-2011. *Antarctic Science* 24:485–499
- 789 Carmona E, Almendros J, Martn R, Corts G, Alguacil G, Moreno J, Martn JB, Martos A,
790 Serrano D, Stich, Ibez J (2014) Advances in seismic monitoring at deception island
791 volcano (antarctica) since the international polar year. *Annals of Geophysics* 57
- 792 Caselli A, Santos-Alfonso M, Agosto MR (2004) Gases fumarolicos de la isla Decepcion
793 (Shetland del Sur, Antartida): Variaciones quimicas y depositos vinculados a la crisis
794 sismica de1999. *Asociación Geológica Argentina Revista* 59:291–302
- 795 Caselli A, Badi G, Bonatto AL, Bengoa CL, Agosto MR, Bidone A, Ibáñez J (2007) Ac-
796 tividad sísmica y composición química fumarólica anómala debido a posible efecto sello
797 en el sistema volcánico, Isla Decepción (Antártida). *Revista de la Asociación Geológica*
798 *Argentina* 62:545–552
- 799 Catalan M, Agudo LM, Muoz-Martin A (2006) Geomagnetic secular variations of Bransfield
800 Strait (Western Antarctica) from analysis of marine crossover data. *Geophysical Journal*
801 *International* 165:73–86
- 802 Chouet B (2003) Volcano seismology. *PAGEOPH* 160:739–788
- 803 Cooper AP, Smellie JL, Maylin J (1999) Evidence for shallowing and uplift from bathymetric
804 records of Deception Island, Antarctica. *Antarctic Science* 10:455–461
- 805 De Siena L, Del Pezzo E, Bianco F, Tramelli A (2009) Multiple resolution seismic attenuation
806 imaging at Mt. Vesuvius. *Physics of the Earth and Planetary Interiors* 173:17–32

- 807 De Siena L, Del Pezzo E, Bianco F (2010) Seismic attenuation imaging of Campi Flegrei:
808 Evidence of gas reservoirs, hydrothermal basins and feeding systems. *Journal of Geo-*
809 *physical Research* 115
- 810 De Siena L, Del Pezzo E, Thomas C, Curtis A, Margerin L (2013) Seismic energy envelopes
811 in volcanic media: in need of boundary conditions. *Geophysical Journal International*
812 195 (2):1102–1119
- 813 De Siena L, Thomas C, Aster R (2014) Multi-scale reasonable attenuation tomography
814 analysis (MuRAT): an imaging algorithm designed for volcanic regions. *Journal of Vol-*
815 *canology and Geothermal Research* 277:22–35
- 816 Del Pezzo E, Bianco F, De Siena L, Zollo A (2006) Small scale shallow attenuation structure
817 at Mt. Vesuvius. *Physics of the Earth and Planetary Interiors* 157:257–268
- 818 Eberhart-Phillips D, Reyners M, Chadwick M, Stuart G (2008) Three-dimensional atten-
819 uation structure of the Hikurangi subduction zone in the central North Island, New
820 Zealand. *Geophysical Journal International* 174:418–434
- 821 Fernández-Ibáñez F, Pérez-López R, Martínez-Díaz JJ, Paredes C, Giner-Robles J, Caselli
822 A, Ibáñez J (2005) Costa Recta Beach, Deception Island, West Antarctica: a retreated
823 scarp of a submarine fault. *Antarctic Science* 17:418–426
- 824 García-Yeguas A, Almendros J, Abella R, Ibáñez J (2010) Quantitative analysis of seismic
825 wave propagation anomalies in azimuth and apparent slowness at Deception Island
826 volcano (Antarctica) using seismic arrays. *Geophysical Journal International* pp doi:
827 10.1111/j.1365-246X.2010.04,864.x
- 828 Haberland C, Rietbrock A (2001) Attenuation tomography in the western central Andes: A
829 detailed insight into the structure of a magmatic arc. *Journal of Geophysical Research*
830 106(B6):11,151–11,167
- 831 Hansen S, Thurber CH, Mandernach M, Haslinger F, Doran C (2004) Seismic Velocity
832 and Attenuation Structure of the East Rift Zone and South Flank of Kilauea Volcano,
833 Hawaii. *Bulletin of the Seismological Society of America* 94:1430–1440
- 834 Hunsen S, Smith RB, Waite GP (2004) Evidence for gas and magmatic sources beneath
835 Yellowstone volcanic field from seismic tomographic imaging. *Journal of Volcanology*
836 *and Geothermal Research* 131:397–410
- 837 Ibáñez J, Almendros J, Alguacil G, Morales J, Del Pezzo E, Ortiz R (1997) Eventos ssmicos
838 de largo periodo en la isla de Deception: evidencias de una zona volcánica activa. *Boletín de*
839 *la RSEHN* 93:103–110
- 840 Ibáñez J, Del Pezzo E, Morales J, Alguacil G, Almendros J, Ortiz R, La Rocca M, García
841 A (2000) Seismovolcanic signals at Deception Island Volcano, Antarctica: wave field
842 analysis and source modelling. *Journal of Geophysical Research* 135:13,905–13,931
- 843 Ibáñez J, Carmona E, Almendros J, Saccorotti G, Del Pezzo E, Abril M, Ortiz R (2003) The
844 1998–1999 seismic series at Deception Island volcano, Antarctica. *Journal of Volcanology*
845 *and Geothermal Research* 128:65–88
- 846 Julian BR, Ross A, Foulger GR, Evans JR (1996) Three-dimensional seismic image of a
847 geothermal reservoir: the Geysers, California. *Geophysical Research Letters* 23:685–688
- 848 Julian BR, Pitt A, Foulger GR (1998) Seismic image of CO₂ reservoir beneath a seismically
849 active volcano. *Geophysical Journal International* 133:F7–F10
- 850 Koulakov I, Bindi D, Parolai S, Grosser H, Milkereit C (2010) Distribution of Seismic Ve-
851 locities and Attenuation in the Crust Beneath the North Anatolian Fault (Turkey)
852 from Local Earthquake Tomography. *Bulletin of the Seismological Society of America*
853 100(1):207–224
- 854 Kusakabe M, Nagao K, Ohba T, Hun Seo J, Park S, Lee J, Park B (2009) Noble gas and
855 stable isotope geochemistry of the thermal fluids from Deception Island, Antarctica.
856 *Antarctic Science* 21:255–267
- 857 Kuznetsov P, Koulakov I (2014) The three-dimensional structure beneath the Popocatepetl
858 volcano (Mexico) based on local earthquake seismic tomography. *Journal of Volcanology*
859 *and Geothermal Research* 276:10–21
- 860 La Rocca M, Del Pezzo E, Simini M, Scarpa R, De Luca G (2001) Array analysis of seis-
861 mograms for explosive sources: evidence for surface waves scattered at the main topo-
862 graphical features. *Bulletin of the Seismological Society of America* 91:219–231
- 863 Lees JM, Lindley GT (1994) Three-dimensional Attenuation Tomography at Loma Prieta:
864 Inverting t^* for Q . *Journal of Geophysical Research* 99(B4):6843–6863

- 865 Luzón F, Almendros J, García-Jerez A (2011) Shallow structure of Deception Island, Antarc-
866 tica, from correlations of ambient noise on a set of dense seismic arrays. *Geophysical*
867 *Journal International* 185:737–748
- 868 Maestro A, Somoza L, Rey J, Martínez-Fras J, López-Martínez J (2007) Active tectonics, fault
869 patterns and stress field of Deception Island: a response to oblique convergence between
870 the Pacific and Antarctic plates. *Journal of South American Earth Sciences* 23:256–268
- 871 Martí J, Vila J, Rey J (1996) Deception Island (Bransfield Strait, Antarctica): an example of
872 a volcanic caldera development by extensional tectonics. McGuire, W J, Jones, A P and
873 Neubeck, J, eds *Volcano instability on the Earth and other planets* Special Publication
874 of the Geological Society, London 110:253–265
- 875 Martí J, Geyer A, Aguirre-Díaz G (2013) Origin and evolution of the Deception Island
876 caldera (South Shetland Islands, Antarctica). *Bulletin of Volcanology* 75:732–750
- 877 Muñoz Martín A, Catalan M, Martín J, Carbo A (2005) Upper structure of Deception Island
878 area (Bransfield Strait, Antarctica) from gravity and magnetic modelling. *Antarctic*
879 *Science* 17:213–224
- 880 Martínez-Arevalo C, Bianco F, Ibáñez J, Del Pezzo E (2003) Shallow seismic attenuation and
881 shear-wave splitting in the short-period range of Deception Island volcano (Antarctica).
882 *Journal of Volcanology and Geothermal Research* 128:89–113
- 883 Matsumoto S, Uehira K, Watanabe A, Goto K, Iio Y, Hirata N, Okada T, Takahashi H,
884 Shimizu H, Shinohara M, Kanazawa T (2009) High resolution Q^{-1} estimation based
885 on extension of coda normalization method and its application to P-wave attenuation
886 structure in the aftershock area of the 2005 West Off Fukuoka Prefecture Earthquake
887 (M 7.0). *Geophysical Journal International* 179:1039–1054
- 888 Melo R, Vieira G, Caselli A, Ramos M (2012) Susceptibility modelling of hummocky terrain
889 distribution using the information value method (Deception Island, Antarctic Penin-
890 sula). *Geomorphology* 155–156:88–95
- 891 Morozov IB (2011) Mechanisms of geometrical seismic attenuation. *Annals of Geophysics*
892 54(3)
- 893 Muksin U, Haberland C, Bauer K, Weber M (2013) Three-dimensional upper crustal
894 structure of the geothermal system in Tarutung (North Sumatra, Indonesia) re-
895 vealed by seismic attenuation tomography. *Geophysical Journal International* 195, doi:
896 10.1093/gji/ggt383:2037–2049
- 897 Ortiz R, García A, Aparicio A, Blanco I, Felpeto A, Del Rey R, Villegas MT, Ibáñez J,
898 Morales J, Del Pezzo E, Olmedillas J, Astiz MM, Vila J, Ramos M, Viramonte JG,
899 Risso C, Caselli A (1997) Monitoring of the volcanic activity of Deception Island, south
900 Shetland Islands, Antarctica (1986–1995). In: Ricci, CA (Ed) *The Antarctic Region: Ge-
901 ological Evolution and Processes*, Terra Antarctica Publications, Siena pp pp. 1071–1076
- 902 Pedrera A, Ruiz-Constán A, Heredia N, Galindo-Zaldívar J, Bohoyo F, Marín-Lechado C,
903 Ruano P, Somoza L (2012) The fracture system and the melt emplacement beneath the
904 Deception Island active volcano, South Shetland Islands, Antarctica. *Antarctic Science*
905 24:173–182
- 906 Prates G, Berrocoso M, Fernández-Ros A, Garca A (2013) Enhancement of sub-daily position-
907 ing solutions for surface deformation monitoring at Deception volcano (south Shetland
908 islands, Antarctica). *Bulletin of Volcanology* 75:1–10
- 909 Priyono A, Suantika G, Widiyantoro S, Nugraba AD (2011) Three-dimensional seismic at-
910 tenuation structure of Mt. Guntur, West Java, Indonesia. *International Journal of To-
911 mography and Simulation* 17:17–28
- 912 Prudencio J, Ibáñez J, García-Yeguas A, Del Pezzo E (2013) Spatial distribution of intrinsic
913 and scattering seismic attenuation in active volcanic islands, II: Deception Island images.
914 *Geophysical Journal International* 195 (3):1957–1969, doi: 10.1093/gji/ggt360
- 915 Saccorotti G, Almendros J, Carmona E, Ibáñez J, Del Pezzo E (2001) Slowness Anoma-
916 lies from two dense seismic arrays at Deception Island volcano, Antarctica. *Bulletin of*
917 *Seismological Society of America* 91:561–571
- 918 Sato H, Fehler MC, Maeda T (2012) *Seismic Wave Propagation and Scattering in the het-
919 erogeneous Earth: Second Edition*. Springer, New York, USA
- 920 Schurr B, Asch G, Rietbrock A, Trumbull R, Haberland CH (2003) Complex patterns of
921 fluid and melt transport in the central Andean subduction zone revealed by attenuation
922 tomography. *Earth and Planetary Science Letters* 215:105–119

- 923 Smellie JL (2001) Lithostratigraphy and volcanic evolution of Deception Island, South Shetland
924 islands. *Antarctic Science* 13:118–209
- 925 Smellie JL, López-Martínez J, Headland RK, Hernández-Cifuentes F, Maestro A, Millar
926 IL, Thomson JW (2002) *Geology and geomorphology of Deception Island*. Cambridge,
927 British Antarctic Survey, p 77p
- 928 Takanami T, Selwyn Sacks I, Hasegawa A (2000) Attenuation structure beneath the volcanic
929 front in northeastern Japan from broad-band seismograms. *Physics of the Earth and
930 Planetary Interior* 121:339–357
- 931 Tejedo P, Gutierrez B, Pertierra LR, Benayas J (2014) Analysis of published scientific
932 research from Deception Island, South Shetland Islands. *Antarctic Science* p
933 doi:10.1017/S0954102014000455
- 934 Torrecillas C, Berrocoso M, Pérez-López R, Torrecillas M (2012) Determination of volumetric
935 variations and coastal changes due to historical volcanic eruptions using historical
936 maps and remote-sensing at Deception Island (West-Antarctica). *Geomorphology* 136:6–
937 14
- 938 Torrecillas C, Berrocoso M, Felpeo A, Torrecillas M, García A (2013) Reconstructing
939 palaeo-volcanic geometries using a Geodynamic Regression Model (GRM): Application
940 to Deception Island Volcano (South Shetland Islands, Antarctica). *Geomorphology*
941 182:79–88
- 942 Vanorio T, Virieux J, Capuano P, Russo G (2005) Three-dimensional tomography from P
943 wave and S wave microearthquake travel times and rock physics characterization of the
944 Campi Flegrei Caldera. *Journal of Geophysical Research*
945 110(B03201):doi:10.129/2004JB003,102
- 946 Vila J, Martí J, Ortiz R, García A, Correig AM (1992) Volcanic tremors at Deception Island,
947 South Shetland Islands, Antarctica. *Journal of Volcanology and Geothermal Research*
948 53:1–4
- 949 Vila J, Correig AM, Martí J (1995) Attenuation source parameters at Deception Island
950 (South Shetland Islands, Antarctica). *Pure and Applied Geophysics* 144:229–250
- 951 Yoshimoto K, Sato H, Ohtake M (1993) Frequency-dependent attenuation of P and S waves
952 in Kanto area, Japan, based on the coda-normalization method. *Geophysical Journal
953 International* 114:165–174
- 954 Zandomenighi D, Barclay A, Almendros J, Ibáñez J, Wilcock WSD (2009) Crustal structure
955 of Deception Island volcano from P-wave seismic tomography: tectonic and volcanic
956 implications. *Journal of Geophysical Research* 114

Fig1

[Click here to download Figure: Fig1.eps](#)

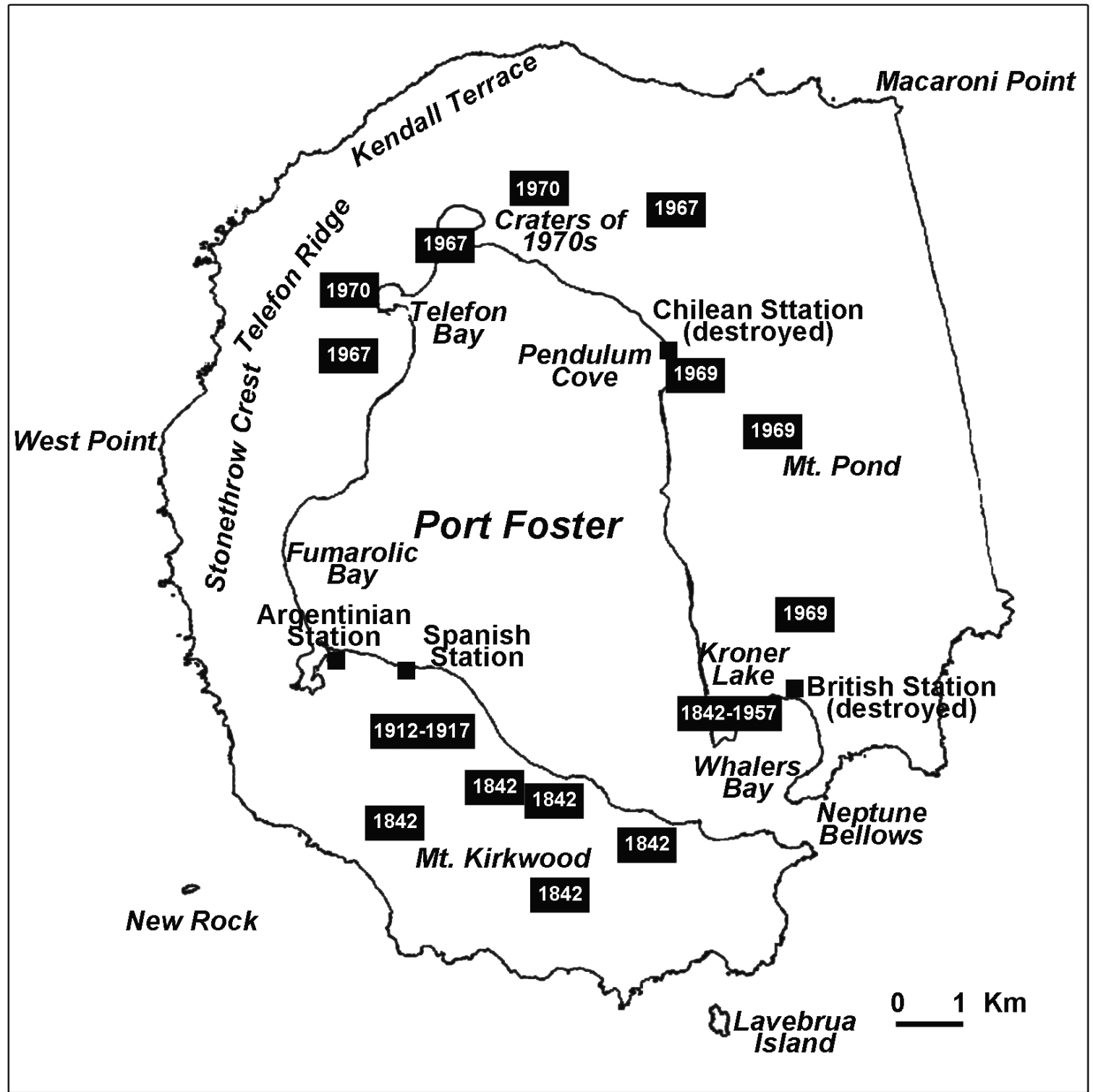
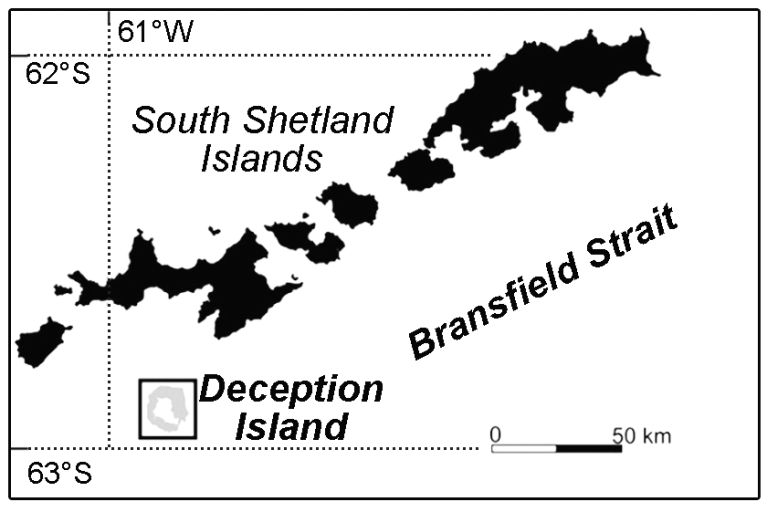
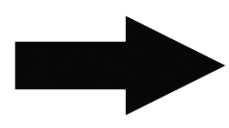
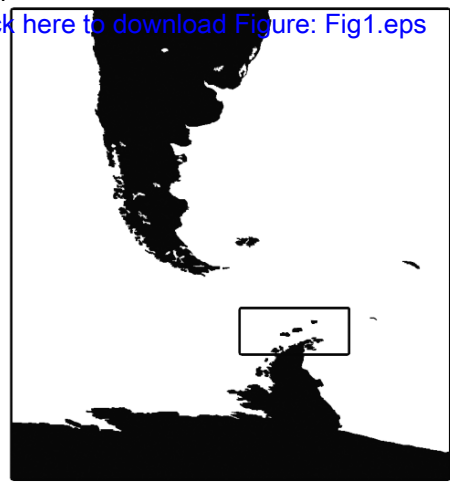


Fig2

[Click here to download high resolution image](#)

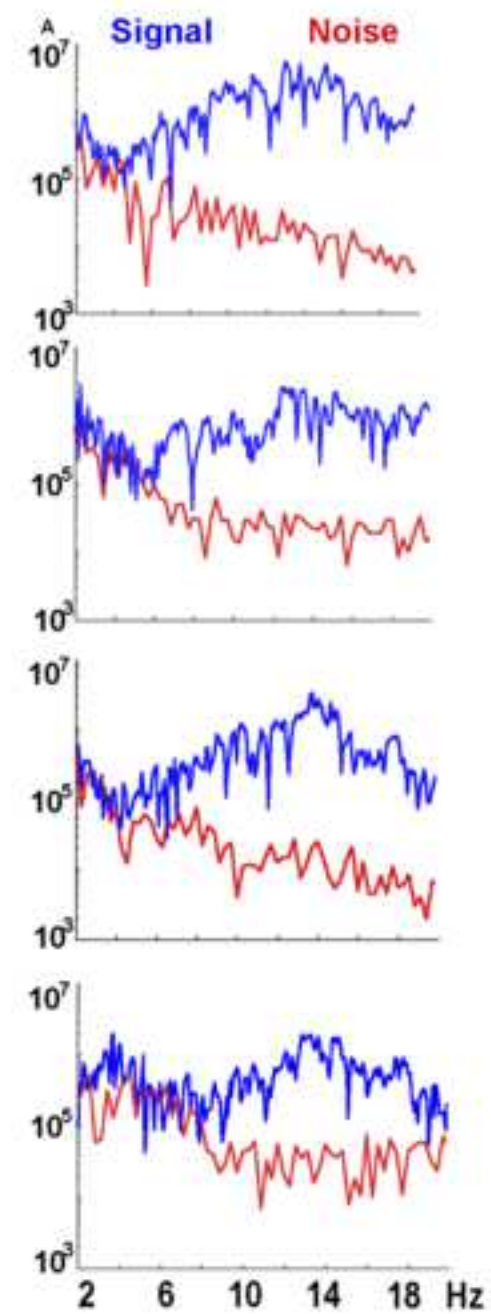
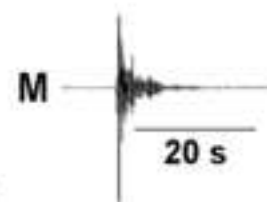
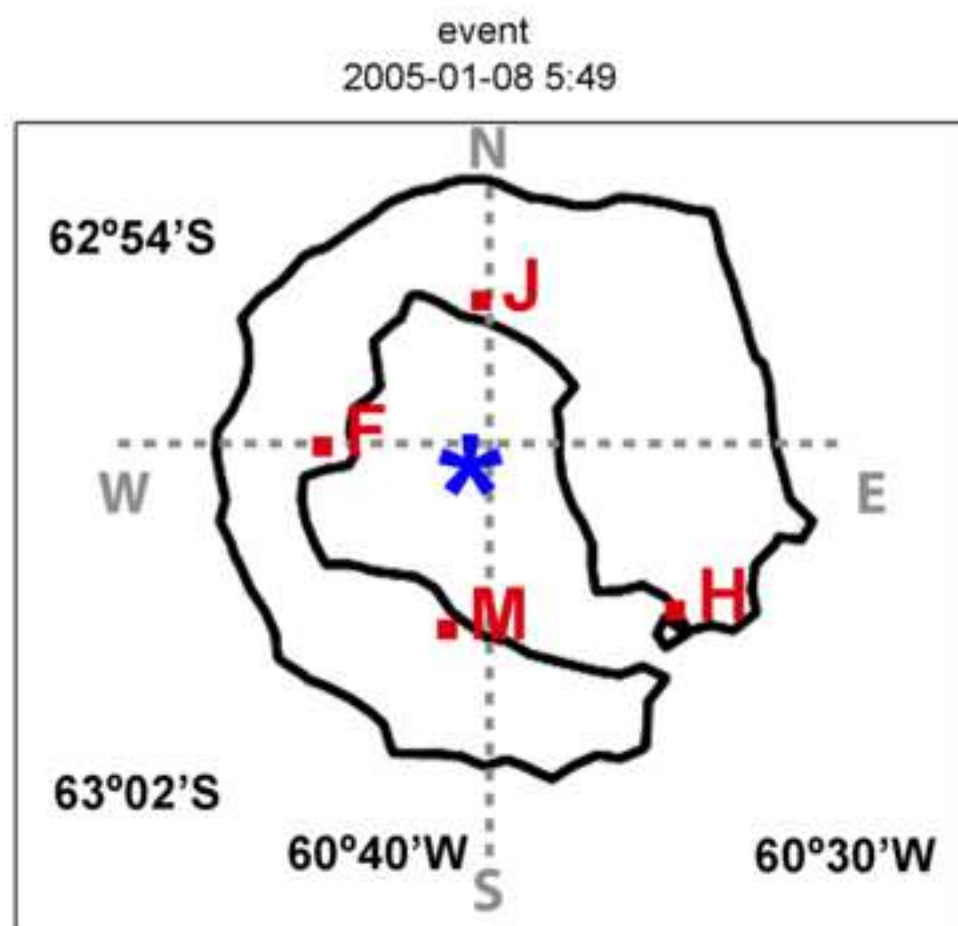


Fig3

[Click here to download high resolution image](#)

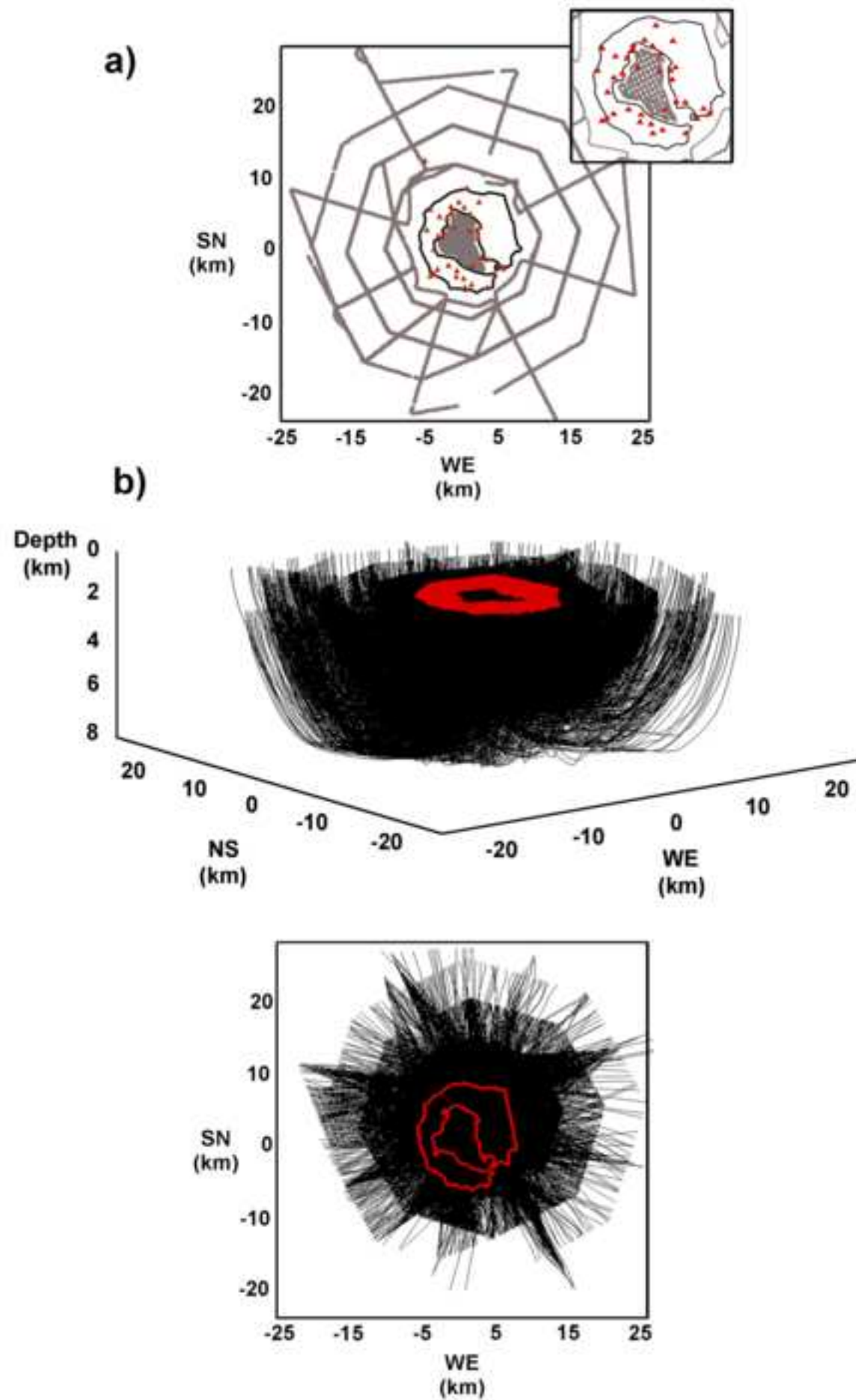


Fig4

[Click here to download high resolution image](#)

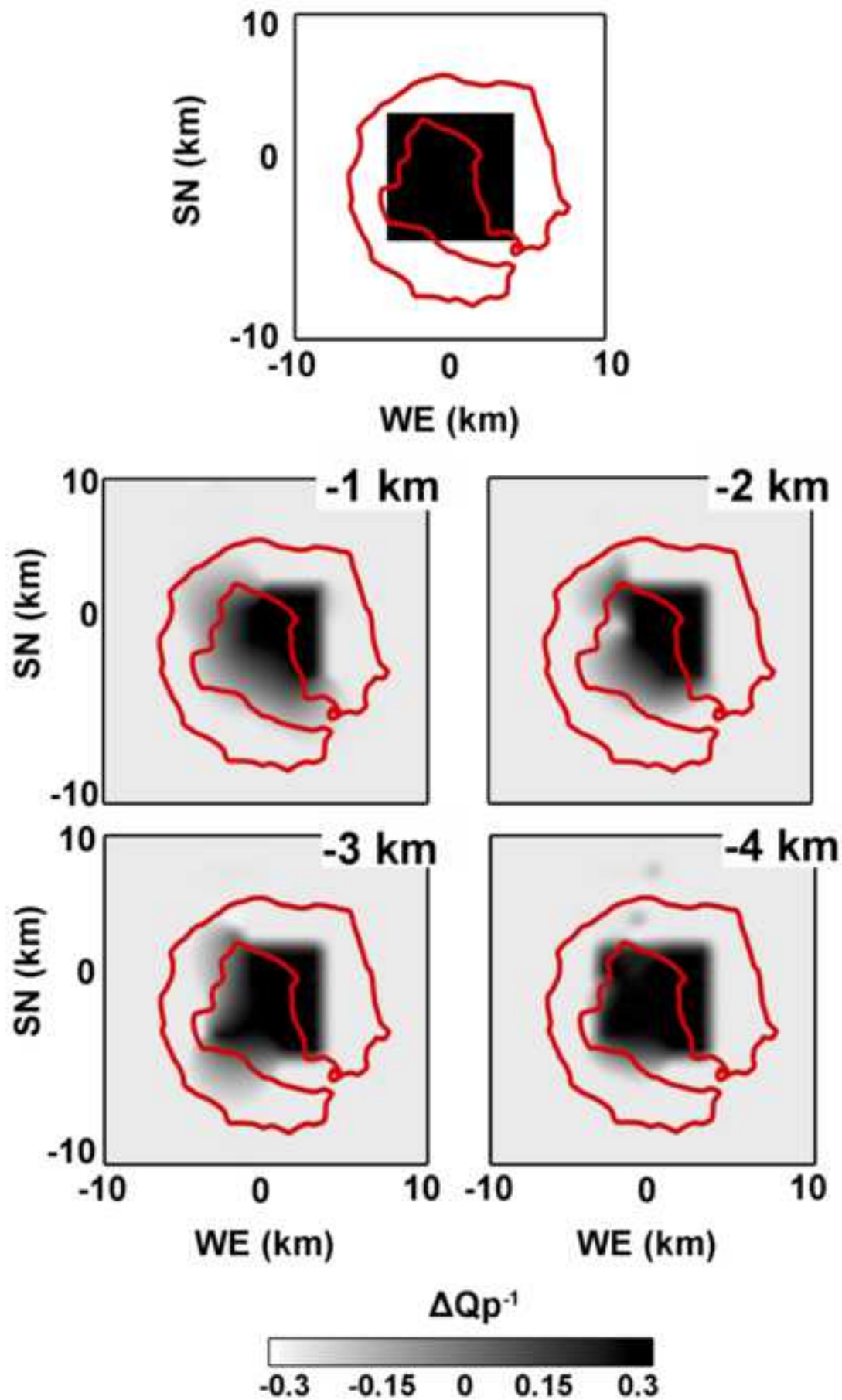


Fig5

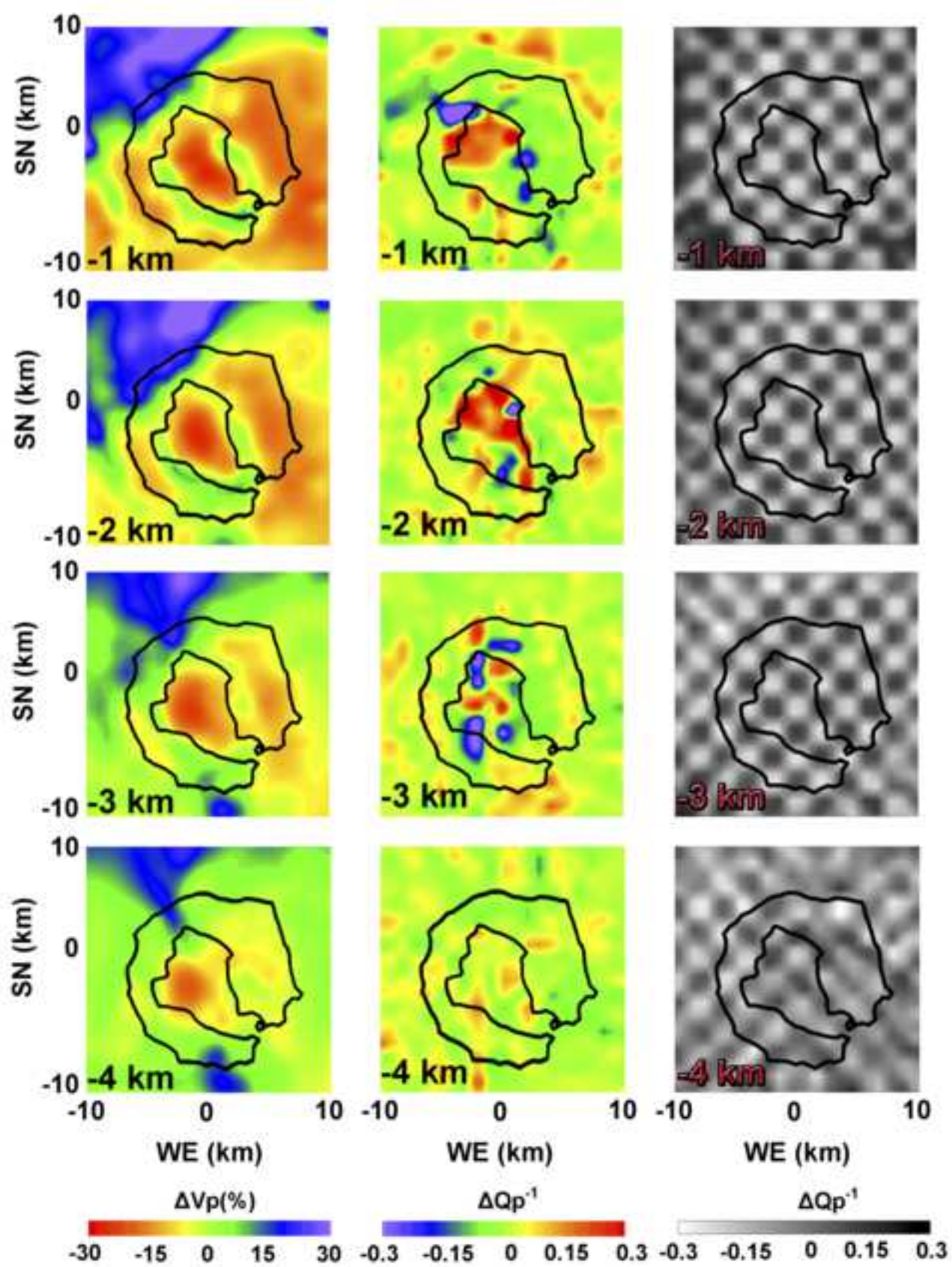
[Click here to download high resolution image](#)

Fig6

[Click here to download high resolution image](#)